

Chemical modifications for water-repellent coatings on engineering metals

by

©Boyang Gao

A thesis submitted to the School of Graduate Studies in partial fulfillment of the requirements for the degree of

Master of Science

Department of Chemistry

Memorial University of Newfoundland

September 2018

St. John's

Newfoundland

Abstract

Hydrophobic surfaces have drawn lots of attention for use in applications such as self-cleaning surfaces, anti-icing in harsh environments and corrosion resistance. Generally speaking, the prerequisite for hydrophobic surface synthesis is the combination of micro-scale and nano-scale surface structures along with a low surface energy coating. In my research work, chemical methods were investigated to produce hydrophobic carbon steel and stainless steel, which are important engineering metals.

Simple chemical etching and organic coatings were applied to carbon steel and stainless steel. Although the hydrophobicity of the modified surface increased, the degree of water repellency didn't reach our expectation. Furthermore, the heterogeneous etching and coating caused large uncertainty in terms of wettability. The most promising system is a zinc electrodeposit with a stearic acid coating. We showed that mildly alkaline electrolytes can be used for the fabrication of zinc coatings that give rise to remarkably low adhesion surfaces. Various parameters (pH, applied potential, electrolyte composition) during zinc electrodeposition influenced the homogeneity of zinc coverage and the topography of zinc crystalites, which consequently impacted the hydrophobicity of the surface. Moreover, the two important roles of stearic acid, preventing the oxidation of zinc surface and decreasing the surface energy, were also studied. In conclusion, the zinc layer not only increases the roughness of the surface, but also provide excellent adhesion to the organic coating.

Acknowledgements

I would like to thank my supervisor Dr. Kristin M. Poduska for her expert advice and constant encourage during the process of my thesis work. I would also like to thank Dr. Xili Duan for his extraordinary support for my research project.

I would like to thank my colleagues and friends for their wonderful collaboration and brilliant ideas. Without your support, I can't make such impressive achievements in my research work.

This project would have been impossible without the financial support from Petroleum Research Newfoundland & Labrador (PRNL). Moreover, I especially want to thank the Chemistry Department at Memorial University for providing excellent resources to support my research.

Table of Contents

Abstract	ii
Acknowledgments	iii
Table of Contents	vii
List of Tables	viii
List of Figures	xiii
List of Abbreviations and Symbols	xiii
1 Introduction	1
1.1 Wettability	1
1.1.1 Surface energy and surface tension	2
1.1.2 Contact angle	3
1.1.3 Wenzel model	4
1.1.4 Cassie–Baxter model	5
1.2 Electrodeposition	7
1.3 Organization of thesis	8
2 Experiment details	10

2.1	Zinc electrodeposition and organic coating	10
2.2	Polarization curves	12
2.3	Contact angle measurements	14
2.4	X-ray diffraction	16
2.5	Scanning electron microscopy	17
2.5.1	Secondary electron detection	18
2.5.2	Backscattered electron detection	18
2.5.3	Energy dispersive X-ray (EDX) detection	19
2.6	Attenuated Total Reflectance Fourier transform infrared spectroscopy (ATR-FTIR)	19
2.7	Profilometer measurements	20
3	Wettability studies of steel without electrodeposits	21
3.1	Carbon steel substrate	21
3.1.1	Organic coating	22
3.1.2	Contact angle measurements	24
3.1.3	Polarization curves	25
3.2	Stainless steel substrates	27
3.2.1	Chemical etching	27
3.2.2	Conclusion	29
4	Zinc electrodeposition on carbon steel	33
4.1	Zinc electrodeposition	33
4.2	Zinc film deposition on carbon steel	34
4.2.1	Polarization curves	35
4.2.2	Dodecanethiol (DDT) coatings	36
4.2.3	Stearic acid coatings	36

4.3	Zinc deposition on stainless steel bars	39
4.3.1	Modification of the zinc electrodeposition procedure	39
4.4	Mixtures of organic coatings	42
4.5	ATR–FTIR analyses	43
5	Zinc electrodeposits for water repellent surfaces	45
5.1	Introduction	45
5.2	Experimental	47
5.2.1	Electrodeposition	47
5.2.2	Characterization	48
5.3	Results and Discussion	48
5.3.1	Use of surfactant	50
5.3.2	Variation of pH and deposition potential	51
5.3.3	Protection from water and oxidation	53
5.3.4	Interactions with water droplets	56
5.3.5	Discussion of water adhesion on electrodeposits	59
5.4	Conclusions	60
5.5	Supporting information	62
5.5.1	Deposits on larger substrates	62
5.5.2	Optical images of electrodeposits	63
5.5.3	Electron-based characterization	63
5.5.4	Self-cleaning behaviour	63
6	Conclusions and future work	67
6.1	Conclusions	67
6.2	Future work	69

A Studies of other electrodeposits	70
A.1 Calcium phosphate	70
A.1.1 Previous material	70
A.1.2 Experimental section	71
A.1.3 Preliminary results	72
Bibliography	72

List of Tables

3.1	Corrosion parameters for carbon steel with different organic coatings	27
4.1	Corrosion parameters of different zinc coatings	36

List of Figures

1.1	a: A schematic diagram of a droplet on a surface. b: A hydrophilic surface has a contact angle θ smaller than 90° . c: A hydrophobic surface has a contact angle θ larger than 90°	4
1.2	Demonstration of the wettability difference between a hydrophobic low energy surface (Aculon) and a hydrophilic high energy surface (bare steel). Dimensions of the bar: 6 mm \times 8 mm \times 50 mm.	5
1.3	A schematic diagram of the homogeneous wetting regime (Wenzel).	5
1.4	A schematic diagram of the heterogeneous wetting regime (Cassie-Baxter).	6
2.1	Schematic diagram of zinc electrodeposition and organic coating process.	11
2.2	Example of a Tafel extrapolation plot.	14
2.3	Contact angle instrument.	15
2.4	Static contact angle (CA) fit applied to a water droplet on a surface. The values of the left and right fits are labeled at the top of the image.	16
2.5	Photograph of ATR-FTIR spectrometer.	20
3.1	a: Photograph of rusted carbon steel. b: Photograph of clean carbon steel. Dimensions of the bars: 6 mm \times 8 mm \times 50 mm.	22

3.2	Photograph of a 5 μL water droplet on carbon steel. The contact angle here is 65° .	23
3.3	a: Photograph of a 5 μL water droplet on dodecanethiol coating. The contact angle here is 92° . b: Photograph of a 5 μL water droplet on 24 h exposed dodecanethiol coating. The contact angle here is 132° .	25
3.4	Static contact angle of three different organic coatings on carbon steel.	26
3.5	Polarization curves for different coating materials on carbon steel. The slope lines indicate the parts of the curves that were fit in order to extract E_{corr} and J_{corr} values.	26
3.6	Static contact angles of 5 μL water droplets on bare stainless steel after different chemical etching treatments.	30
3.7	Static contact angles of 5 μL water droplets on stearic acid-coated stainless steel after different chemical etching treatments.	31
3.8	Static contact angles of 5 μL water droplets on Aculon-coated stainless steel after different chemical etching treatments.	32
4.1	Polarization curves for zinc electrodeposits prepared at different pH values.	35
4.2	These representative photos show water droplets on dodecanethiol coated zinc surfaces. a: maximum contact angle value ($134\pm 2^\circ$), and b: minimum contact angle value ($128\pm 1^\circ$).	37
4.3	Photograph of stearic acid coated zinc film on carbon steel, and an image of a 5 μL water droplet on the surface.	38
4.4	A series of snapshots of a water droplet rolling off the surface of a galvanostatically produced zinc film with stearic acid coating.	38

4.5	Photograph of a: no zinc layer on stainless steel, and b: zinc deposit that is partially rinsed off of the stainless steel. Dimensions of the bars: 6 mm × 8 mm × 50 mm.	39
4.6	Photograph of a uniform zinc film on a stainless steel bar. Dimensions of the bar: 6 mm × 8 mm × 50 mm.	41
4.7	A series of snapshots of a water droplet rolling off a potentiostatically produced zinc electrodeposit with stearic acid coating on stainless steel substrate.	41
4.8	Static contact angles of 5 μL water droplets on zinc films with different organic coatings.	42
4.9	ATR-FTIR of white deposits scraped from the stainless steel substrate during early stages of zinc electrodeposition. Peaks are likely related to N-H and N-O species.	44
5.1	Representative XRD data for a Zn electrodeposit prepared at optimized deposition conditions (pH = 8, $E = -1.5$ V) and then coated with stearic acid. The hkl indices correspond to the unit cell for hexagonal Zn (JCPDS 98-000-0482), asterisk (*) denotes peaks due to the stainless steel substrate, and plus (+) denotes a peak related to stearic acid.	49
5.2	Representative SEM images of Zn electrodeposits (a) with PEI surfactant and (b) without surfactant. Scale bars for both images are 2 μm , and both samples were prepared at -1.5 V and pH = 8.	51
5.3	Representative XRD data for a water-rinsed electrodeposit that shows evidence of $\text{Zn}_5(\text{OH})_8\text{Cl}_2(\text{H}_2\text{O})$ (JCPDS 98-000-7203) in addition to metallic Zn (JCPDS 98-000-0482).[92] The asterisk (*) denotes peaks due to the stainless steel substrate, and plus (+) denotes a peak related to stearic acid.	54

5.4	Representative profilometer scans of (a) bare stainless steel (black), ethanol-rinsed electrodeposit (red), and water-rinsed electrodeposit (blue). Corresponding root-mean-square (rms) roughness values are (in units of μm): 1.0 ± 0.3 , 2.0 ± 0.9 , and 4.0 ± 0.8 . In (b), four different scans of a single water-rinsed electrodeposit are compared. Corresponding root-mean-square (rms) roughness values are (in units of μm): 2 ± 1 , 4 ± 1 , 5 ± 2 , and 8 ± 4	55
5.5	Representative image sequences of water droplets being moved across electrodeposit surfaces. For (a-c), a water droplet at the end of a syringe is brought into contact and then lifted from the electrodeposit. For (d-f), a similar droplet was slid across the surface without sticking. For (g-i), a sliding droplet was pinned to an inhomogeneity on the electrodeposit and was detached from the syringe needle.	58
5.6	Representative SEM images of Zn electrodeposits. At constant deposition potential (-1.5 V), more alkaline pH values ((a) at 7.5) affect size and shape relative to more neutral pH ((b) at 8.0 and (c) at 8.5). Keeping the same pH value (8.0) and making the deposition potential less negative leads to more uniform crystallite sizes and shapes ((d) at -1.5 V, (e) at -1.4 V, (f) at -1.3 V). Scale bars for all SEM images are $2 \mu\text{m}$	61
5.7	Photographs of a: zinc electrodeposit on stainless steel (-1.3 V), and b: zinc electrodeposit on stainless steel (-1.5 V). Dimensions of the plates: 3 cm x 3 cm.	62
5.8	Optical images of a: optimized zinc coating, and b: oxidized zinc coating. Dimensions of the plates: 3 cm x 3 cm.	64

5.9	Representative back scattered electron images and energy-dispersive X-ray data for a: optimized zinc coating, and b: oxidized zinc coating.	65
5.10	Consecutive images: the self-cleaning behaviour of our zinc coating.	66
A.1	Photograph of a 5 μ L water droplet on (a): bare stainless steel (contact angle = $79 \pm 1^\circ$), and (b): calcium phosphate electrodeposit (contact angle = $127 \pm 1^\circ$).	71
A.2	Photograph of calcium phosphate electrodeposit.	72

List of Abbreviations and Symbols

ACP	ACP chemical company
ACS	American Chemical Society
ATR	attenuated total reflectance spectroscopy
BSE	backscattered electron
BSED	backscattered electron detection
CA	contact angle
CE	counter electrode
DDT	dodecanethiol
E	electrode potential (V)
E_{corr}	corrosion potential (V)
EDX	energy dispersive X-ray
FTIR	Fourier-transform infrared spectroscopy
I	measured current (A)
I_{corr}	corrosion current (A)
j_{corr}	corrosion current density (i/Acm^{-2})
I_{oe}	reaction dependent exchange current
RE	reference electrode
S	spreading parameter
SCE	saturated calomel electrode
SEI	secondary electron imaging

SEM	scanning electron microscopy
STA	stearic acid
WE	working electrode
XRD	X-ray diffraction
$\gamma_{solid/gas}$	interfacial energy between air and solid (J/m ²)
$\gamma_{solid/liquid}$	interfacial energy between solid and liquid (J/m ²)
$\gamma_{liquid/gas}$	interfacial energy between liquid and gas (J/m ²)
θ	contact angle (°)
γ_{SV}	interfacial energy between vapour and solid (J/m ²)
γ_{SL}	interfacial energy between solid and liquid (J/m ²)
γ_{LV}	interfacial energy between liquid and vapour (J/m ²)
θ_A	observed contact angle (°)
θ_C	contact angle of smooth surface (°)
r	roughness factor (μm)
ϕ_s	area fraction of the substrate in contact with the liquid droplet
β	Tafel constant
β_a	anodic Tafel constant
β_b	cathodic Tafel constant
λ	wavelength of X-ray (nm)
n	diffraction order
d	lattice spacing
hkl	Miller indices

Chapter 1

Introduction

This introductory chapter gives an overview of simple water wetting phenomena and models, as well as an introduction to electrochemical metal deposition. Both of these are large topics and have been the focus of many recent review articles. [1–4]

1.1 Wettability

In recent years, hydrophobic materials have been of great interest for industrial applications, such as self-cleaning [5], drag reduction in fluids [6], anti-icing in harsh environments [7,8] and corrosion resistance [9], especially for superhydrophobic metals [10], which can be used in aeronautics [11], and offshore pipelines [12]. Inspired by nature such as the lotus leaf [13], wettability is understood through aspects of surface structure and surface energy. Therefore, to fabricate a water repellent surface, we need to learn about some background knowledge of surface energy and surface structure.

1.1.1 Surface energy and surface tension

Surface energy is also called interfacial free energy, which is defined as the excess energy at a surface compared to the bulk [14]. For instance, consider a water droplet in the air. An inner water molecule is pulled in all directions by the surrounding water molecules, which results in the net force on this inner water molecule to be zero. The attractive force generated between molecules of the same type is called the cohesive force. However, for molecules on the surface, they don't have the same number of water molecules on all sides. Moreover, air molecules also possess a tendency to attract the surface water molecules. This sort of attractive force between molecules of different types is called the adhesive force. Due to the relatively low density of air compared to water, the cohesive force is larger than adhesive force. Thus, the surface water molecules are pulled inwards and the net force of surface water molecules is not zero. The dimension of surface tension is either force per unit length, or energy per unit area. Therefore, surface tension is also used for surface energy. Surface molecules contain more energy than molecules in the bulk. Similarly, solid substrates also have surface energy, which is the interfacial energy between air and solid ($\gamma_{solid/gas}$) [15]. If the surface energy of a solid substrate changes due to the addition of a liquid droplet on the surface, the surface is said to be wetting. The spreading parameter [16] can be used to explain this situation, as shown in Equation 1.1:

$$S = \gamma_{solid/gas} - \gamma_{solid/liquid} - \gamma_{liquid/gas} \quad (1.1)$$

If $S \geq 0$, the liquid wets the surface completely. If $S \leq 0$, the solid surface is just partially wet. So in other words, surface energy can also be defined as the amount of energy which is used to increase the surface area of the liquid droplet. For a hydrophobic surface, we don't want the liquid to wet the solid surface. Therefore, if a

solid substrate has a low energy surface, which cannot provide enough energy for the increase of liquid surface area [17, 18], then this low energy solid surface can prevent wetting by the liquid. Some substances, such as metal and glass, tend to have high energy surfaces. For other materials, such as fluorocarbons and hydrocarbons, have low energy surfaces since their molecules are connected by weaker forces (hydrogen bonds, van der Waals interactions) [19].

1.1.2 Contact angle

Contact angles can be used to quantify the wetting property of the solid surface. On an ideal solid surface (smooth), Young's equation (Equation 1.2) [20]:

$$\cos \theta = \left(\frac{\gamma_{SV} - \gamma_{SL}}{\gamma_{LV}} \right) \quad (1.2)$$

can be used to express the relation between the contact angle (θ) and three specific interfacial energies. As shown in Figure 1.1a, these three interfacial energies, γ_{SV} (interfacial energy between vapour and solid), γ_{SL} (interfacial energy between solid and liquid) and γ_{LV} (interfacial energy between liquid and vapour), should be balanced in the horizontal direction. Generally speaking, if the contact angle is smaller than 90° , the solid surface is defined as hydrophilic (Figure 1.1b). If the contact angle is larger than 90° , the surface is hydrophobic (Figure 1.1c). The surface is regarded as superhydrophobic surface if the contact angle is larger than 150° [21].

As mentioned above, a low energy surface can better prevent the wetting of a liquid. In Figure 1.2, there is a carbon steel bar with a high energy surface. The right half of this steel was coated by Aculon, which is a commercial organic polymer, and gives a low energy surface. Water droplets were dispensed on each part. It's clear from the contact angle that Aculon gives a low energy surface and the bare steel has

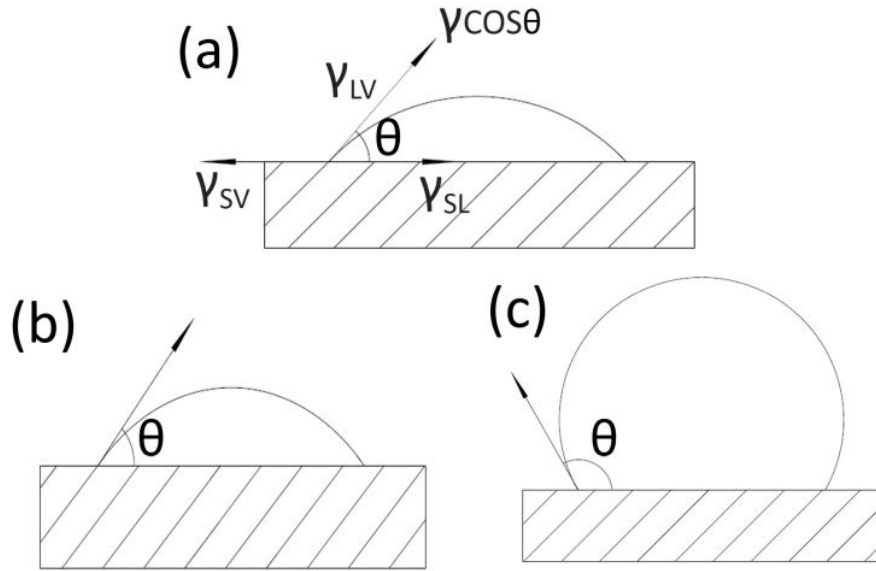


Figure 1.1: a: A schematic diagram of a droplet on a surface. b: A hydrophilic surface has a contact angle θ smaller than 90° . c: A hydrophobic surface has a contact angle θ larger than 90° .

a high energy surface.

1.1.3 Wenzel model

Young's equation has a drawback in that it can only be applied to an ideal smooth surface. But what if the solid substrate has a homogeneous rough surface? As shown in Figure 1.3, the water droplet could penetrate into the grooves. In this case, the contact angle can be explained by the Wenzel model (Equation 1.3) [22]:

$$\cos \theta_A = r \cos \theta_C \quad (1.3)$$

where θ_A is the observed contact angle. r is the roughness factor which is the ratio of the true area of the solid surface to the projected area, and θ_C is the contact angle of the smooth surface. On a rough surface, the true area of the solid surface is larger

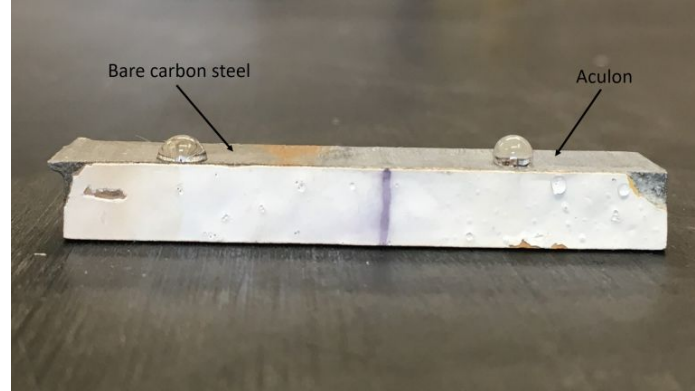


Figure 1.2: Demonstration of the wettability difference between a hydrophobic low energy surface (Aculon) and a hydrophilic high energy surface (bare steel). Dimensions of the bar: 6 mm \times 8 mm \times 50 mm.

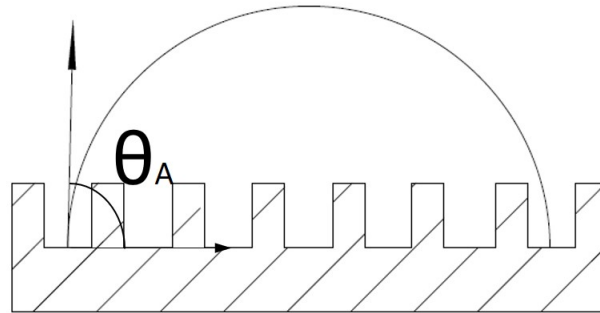


Figure 1.3: A schematic diagram of the homogeneous wetting regime (Wenzel).

than the projected area of the solid surface, which means that r is larger than 1. Thus, based on Equation 1.3, we can conclude that, if the original smooth surface is a hydrophilic surface, then the corresponding rough surface becomes more hydrophilic. Vice versa, if the original smooth surface is a hydrophobic one, then the corresponding rough surface would become more hydrophobic.

1.1.4 Cassie–Baxter model

How about a heterogeneous rough surface? Imagine that if the regularly rough solid substrate has a low surface energy (Figure 1.4), the liquid droplet doesn't penetrate

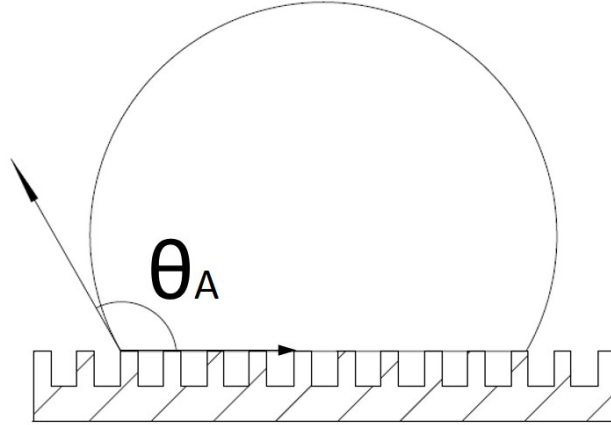


Figure 1.4: A schematic diagram of the heterogeneous wetting regime (Cassie-Baxter).

into these grooves. Instead, some air pockets are trapped in these grooves. In this case, the contact angle can be explained by the Cassie–Baxter model (Equation 1.4) [23,24]:

$$\cos \theta_A = \phi_s(\cos \theta_C + 1) - 1 \quad (1.4)$$

where θ_A is the observed contact angle. ϕ_s is the area fraction of the substrate in contact with the liquid droplet and θ_C is the contact angle of the smooth surface. From the Cassie-Baxter model, we see that droplets will have a higher observed contact angle if less area is in contact with the solid substrate. Moreover, the Cassie-Baxter model tells us that roughness and low surface energy are two key factors for generating hydrophobic materials. But drawbacks of Cassie–Baxter model are still evident. First, the Cassie-Baxter model only applies to a regularly rough surface. Moreover, this model doesn't say anything about the adhesion between the liquid and the solid surface.

1.2 Electrodeposition

Electrodeposition, also known as electroplating, has been investigated for decades. Electrodeposition is an electrochemical process that forms a thin metal layer on a substrate. During the process, an external electrical current is applied in the electrolyte to generate a redox reaction. As for the reduction, the metal cations in the electrolyte gain electrons so that metal adheres to the electrode (substrate). As for the oxidation reaction, normally it is the generation of O_2 from H_2O . During electroplating, many factors have impacts on the deposition of the metal, such as the composition and concentration of the electrolytes solution and the addition of surfactant. Moreover, the evolution of H_2 is one of the reduction processes occurring on the surface of substrate, and H_2 bubbles on the surface highly influence the morphology and the coverage of deposits.

In recent years, various metal electrodeposition procedures have been used to fabricate water repellent surfaces. Generally speaking, metal electrodeposition can be used to create micron scale or nano-scale structure on the surface to increase the roughness. But metal deposits have high surface energy. Thus, what people usually do is to put a low surface energy coating over a metal deposit. As a result, this combination can produce a hydrophobic surface. Some [25] created a water repellent surface on carbon steel using Fe electrodeposition and organic acid coating, with sliding angles of only $2\pm 0.5^\circ$ (Sliding angle is the angle of minimum slope at which a water droplet will roll off.) Fe deposits had micrometer- and nanometer-scale features that increased the surface roughness. Others [26] combined needle shaped CuO deposition with fluoroalkylsilane coating, which generates a low adhesion surface with a sliding angle of only 1° . Moreover, zinc or zinc oxide electrodeposition with organic coatings have also been investigated [27–30], Based on other's work, the morphology of zinc and zinc oxide crystals can change when using different electrolytes. However,

all zinc and zinc oxide crystals have nano or micro-scale features on the surface that increase the surface roughness. Therefore, a very hydrophobic surface can be obtained by putting an organic coating on the zinc or zinc oxide layer. Few papers mention the adhesion behaviour of zinc coatings, which is one point that I will discuss extensively in my thesis.

1.3 Organization of thesis

Chapter 2 introduces some experimental procedures and characterization methods. The general procedures for electrodeposition and polarization curves are described in detail. Some characterization methods, such as contact angle measurement, X-ray diffraction, scanning electron microscopy and attenuated total reflectance infrared spectroscopy are introduced in terms of background knowledge and their basic applications.

In Chapter 3, two basic treatments (organic coating and chemical etching) were investigated to fabricate a hydrophobic surface on engineering metals. First, organic coating and chemical etching were treated separately on carbon steel. Then the combination of chemical etching and organic coating was studied. Static contact angles were the major method used to quantify the wettability of these surfaces.

In Chapter 4, the combination of zinc electrodeposition and organic coating on carbon steel and stainless steel was investigated. This chapter discusses more details about the procedure of electrodeposition. Three different organic coatings were applied to zinc deposits to lower water droplet adhesion.

Chapter 5 discusses the optimization of zinc-stearic acid coatings on stainless steel, and includes important introductory material that complements Chapter 1. In this chapter, X-ray diffraction analyses were used to confirm the formation of zinc.

Scanning electron microscopy was used to observe the morphology of the zinc coatings. Profilometer measurements were used to quantify the roughness of the zinc coatings.

Chapter 6 gives an overall conclusion of my whole research effort and brings up some future work based on my results. The appendix briefly introduces the electrodeposition of calcium phosphate, which is potentially useful as a hydrophobic material.

Chapter 2

Experiment details

In this chapter, several experiments and characterization methods are introduced in terms of their procedures and background knowledge. The procedure of zinc electrodeposition and polarization curve measurements are discussed. For the quantification of wettability, contact angle measurements are introduced to measure the static contact angle. The roughness of our coated samples were analyzed by profilometer measurements. Since we generated water-repellent samples, we needed to further understand the composition and morphology of them. Therefore, X-ray diffraction, attenuated total reflectance infrared spectroscopy and scanning electron microscopy were used to characterize the samples.

2.1 Zinc electrodeposition and organic coating

In Chapter 4 and Chapter 5, zinc electrodeposition is one of the primary steps to fabricate our low adhesion surfaces. Due to the different types of substrates, there are some differences in the procedures that will be mentioned in the corresponding chapters. However, the composition of electrolytes is identical. The electrolyte is prepared with 0.2 M ZnCl_2 (ACS grade, 97.0%, Caledon) and 3.5 M NH_4Cl (ACS

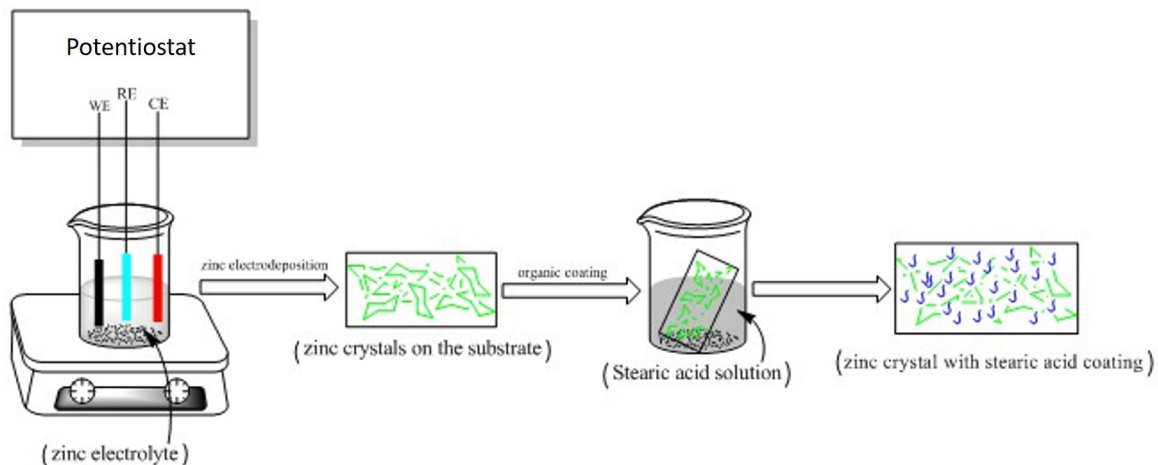


Figure 2.1: Schematic diagram of zinc electrodeposition and organic coating process.

grade, 99.5%, ACP) in ultrapure water (Barnstead, $18.2 \text{ M}\Omega\cdot\text{cm}$). The pH value of the electrolyte is increased to 8 by adding NaOH solid (ACS grade, 97.0%, ACP). We note that precipitates formed when the pH value is near 7, but the precipitates disappear once the pH is increased above 7.5.

As shown in Figure 2.1, electrodeposits are prepared using constant potential or constant current, with steel as the working electrode (WE), a carbon felt or a carbon rod as the counter electrode (CE) and a saturated calomel (SCE) reference electrode (RE). The size of the steel substrates and deposition potentials varied, so more information is mentioned in following chapters. Deposition lasted for 15 min at room temperature while stirring at 200 rpm. After electrodeposition, the sample was immersed in an organic coating solution for a few minutes. For different kinds of organic coatings and substrates, the procedure was varied a little bit and is mentioned in more detail in later chapters. After the sample was taken out from the organic coating solution and dried in air, the surface preparation was complete.

2.2 Polarization curves

The polarization curve method has been widely used for investigating the corrosion resistance of various coatings. When the potential of an electrode is forced away from its open circuit potential, it is referred as polarization [31]. Generally speaking, the polarization of a metal electrode generates current that flows through the electrochemical cell. The corrosion of a metal electrode occurs at the interface between the surface of the metal electrode and the electrolyte. As for the electrochemical reactions during the polarization, one is the anodic reaction (the oxidation of metal by releasing some electrons), and the other one is the cathodic reaction (the reduction of O_2 or H^+ by gaining some electrons) [32]. The corrosion potential (E_{corr}) is obtained when the anodic reaction and the cathodic reaction equilibrate. As shown in Figure 2.2, the horizontal axis shows the potential and the vertical axis shows the logarithm of absolute current. Current at the corrosion potential is called the corrosion current (I_{corr}). By calculating I_{corr} , the corrosion rate can be evaluated. In order to estimate the corrosion rate, the Tafel model is essential for calculating I_{corr} . The prerequisite for using the Tafel model is that the rate of both the anodic and cathodic reaction is controlled by the kinetics of the electron-transfer reactions [33]. The equation of the Tafel model is written as Equation 2.1 [34]:

$$I = I_{oe} \exp \left[\frac{2.303(E - E_{corr})}{\beta} \right]. \quad (2.1)$$

In this equation, I_{oe} is reaction dependent exchange current. E_{corr} is corrosion potential and β is the Tafel constant. The Tafel equation represents half of the redox reaction. However, for corrosion, there are must be two opposing reactions. In this case, the combination of two Tafel equations generates the Butler-Volmer equation

(Equation 2.2 [35]):

$$I = I_{corr} \left(\exp \left[\frac{2.303(E - E_{corr})}{\beta_a} \right] - \exp \left[\frac{2.303(E - E_{corr})}{\beta_c} \right] \right). \quad (2.2)$$

In Butler-Volmer equation, I_{corr} is the corrosion current. β_a is anodic Tafel constant and β_b is cathodic Tafel constant. From the Butler-Volmer equation, when the potential is E_{corr} , the two exponential terms in the equation equal 1. Therefore, the current is zero, which confirms no current at open circuit potential. When the potential is forced away from E_{corr} , one of the exponential terms will dominate more than the other, which means the relation between potential and logarithmic current is the linear region of the polarization curve (Figure 2.2).

As mentioned above, polarization means the potential is forced away from its open circuit potential, so what we investigate is the linear region of the polarization curve. By following the linear regions of both reactions, the intersection point of the two straight lines provides I_{corr} and E_{corr} . Generally speaking, a higher corrosion potential (E_{corr}) and lower corrosion current density reflect a lower corrosion rate and higher corrosion resistance [36]. However, there are many practical factors that impede the extrapolation of linear portions. For instance, during oxidation, the surface of a metal may undergo passivation, which means the surface is changed during the reaction. Moreover, the simultaneous appearance of more than one cathodic reaction (evolution of hydrogen or the reduction of oxygen) also makes the system more complicated [37]. Those factors highlight the difficulty of seeing enough linear portions for extrapolation.

Potentiodynamic polarization curve measurements in this thesis work were executed using a three electrode system with steel as the working electrode, a carbon rod as a counter electrode and a saturated calomel electrode as a reference electrode. In order to mimic the real environment of seawater, the electrolyte was 3.5 wt% NaCl

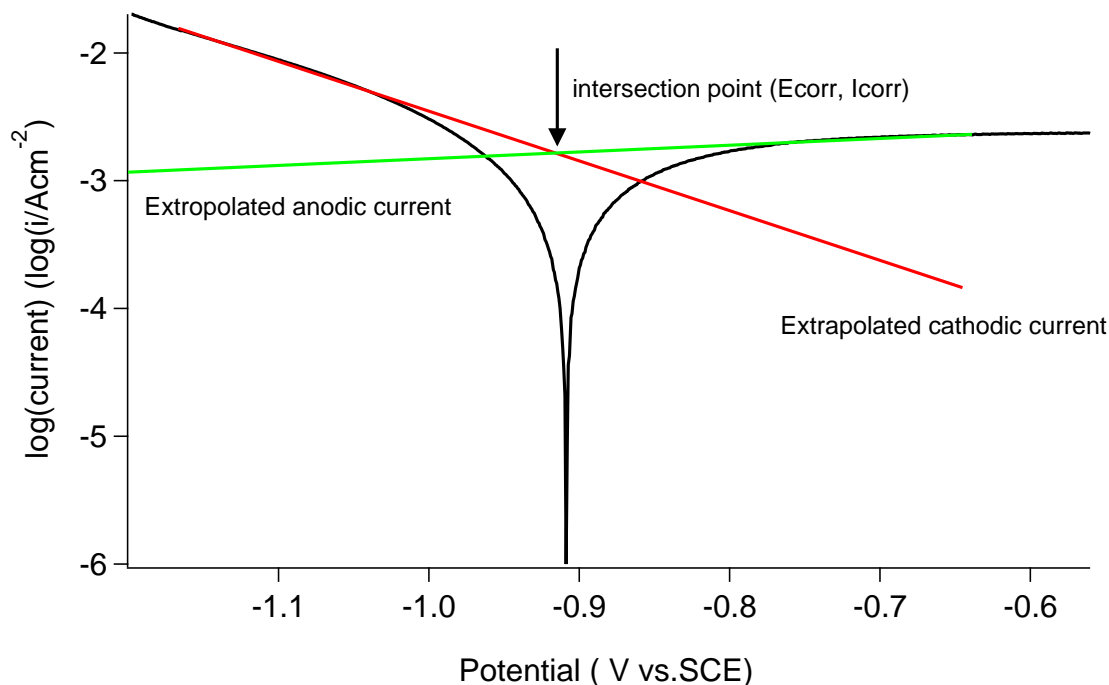


Figure 2.2: Example of a Tafel extrapolation plot.

solution. Before the polarization curve measurement, a 1 cm^2 area of the substrate was immersed in the NaCl solution for 30 min to obtain a stable open circuit potential. For organic coated carbon steel as a substrate, the potential was scanned between -1.2 V and -0.4 V/SCE with a scan rate of 2 mV/s. For zinc coated carbon steel working electrodes, the potential was applied between -1.3 V and -0.4 V/SCE.

2.3 Contact angle measurements

The contact angle measurement is the most common method to quantify the wettability of a surface. Our measurements were done using a OCA 15EC contact angle instrument from Dataphysics (Germany). As shown in Figure 2.3, this instrument has three key components, which are a sample stage, camera and dosing unit. To measure the static contact angle, a sample should be placed horizontally on the sample stage

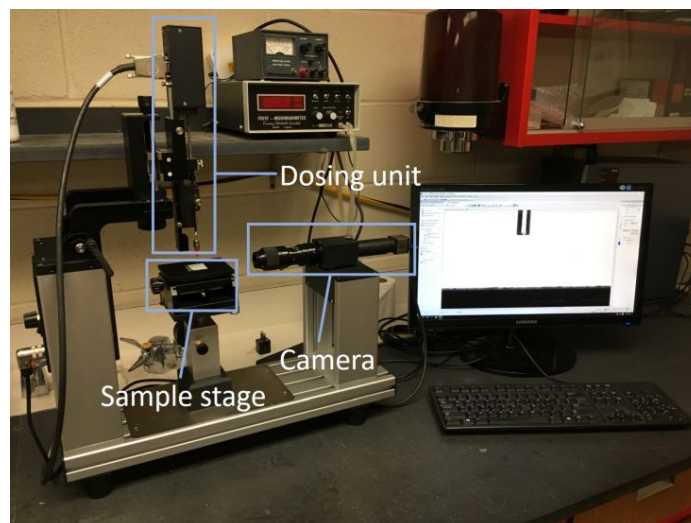


Figure 2.3: Contact angle instrument.

and the camera should be parallel to the surface. The dosing of a droplet is controlled by the software. We select a dispense rate of $2 \mu\text{L}/\text{s}$, and a volume for each droplet of $5 \mu\text{L}$. All the tests were conducted at room temperature ($20 \text{ }^\circ\text{C}$). Normally, a $5 \mu\text{L}$ water droplet is not heavy enough to automatically drop down to the sample. In order to make the droplet touch the surface, we move the needle downward, without touching the needle tip to the solid surface, until the drop settles down to the sample. Then the needle is lifted up while the droplet stays pinned on the surface. The analysis of static contact angle follows three steps (Figure 2.4). First, find the baseline between the water droplet and the surface. Second, detect the drop contour. Third, calculate the contact angle by averaging the left contact angle and the right contact angle of each droplet. All three steps of the analysis are executed automatically by software.

The contact angle values for each sample were averaged based on six different positions on the same sample, to account for possible chemical and topographical inhomogeneities. The error bars shown in each contact angle plot were obtained by calculating the standard deviation of six contact angle values. Under some circum-

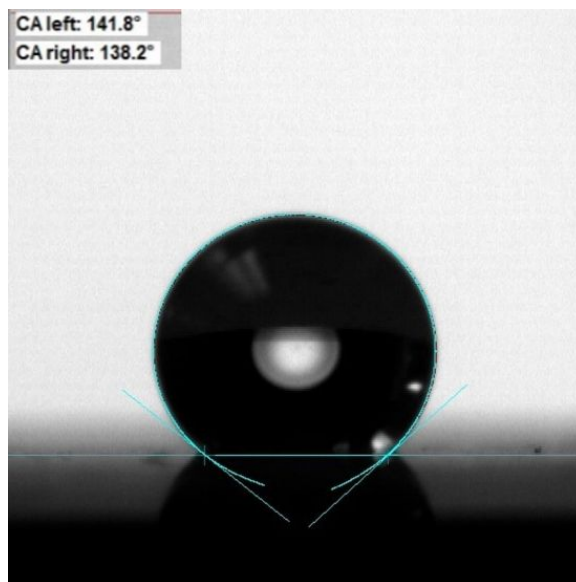


Figure 2.4: Static contact angle (CA) fit applied to a water droplet on a surface. The values of the left and right fits are labeled at the top of the image.

stances (when noted), the volume of each droplet was adjusted to $20 \mu\text{L}$ to measure the contact angle more easily.

2.4 X-ray diffraction

X-ray diffraction (XRD) is appropriate for the characterization of crystalline materials. Three key components made up the instrument: X-ray tube, rotating sample holder and detector [38]. In the X-ray tube, a high energetic electron beam coming from a heating filament strikes a Cu plate. The bombardment of the electron beam on the metal surface forces the ejection of electrons from core shells. Meanwhile, electrons from outer shells fall back to the inner shell and emit radiation (X-ray), so as to fill the vacancy of the inner shell. By using foils or crystal monochromators, a single X-ray wavelength (normally K_{α}) is used. Collimated X-ray beams are directed toward the sample. Meanwhile, the sample holder keeps rotating so that the angle of the incident X-ray beam changes with the rotation of sample holder. The constructive

interference (diffraction) of X-rays occur if the Bragg Equation (2.3) is satisfied [39]:

$$n\lambda = 2d_{hkl} \sin \theta. \quad (2.3)$$

The Bragg equation associates the wavelength of incident X-ray with its incident angle and lattice spacing between atomic planes d_{hkl} . hkl stands for Miller indices which represent specific lattice planes. In a particular crystal system, a number of lattice planes with different Millers indices exist. By scanning the sample while increasing the incident angle (θ), all possible lattice orientations can be detected. The diffracted X-rays are plotted as 2θ versus intensity. Since all the possible lattice planes (d -spacing) can be accessed, the corresponding crystalline solid can be identified by comparison of raw data with standard reference datas and with lattice constant refinements.

In our experiments, XRD analysis was performed using a Rigaku Ultima-IV Powder X-Ray Diffractometer (Cu $K\alpha$, $\lambda = 1.54059 \text{ \AA}$, range $5\text{-}90^\circ$ with 0.02° step size) and lattice constant refinements were obtained using Jade software (Materials Data Inc.)

2.5 Scanning electron microscopy

A scanning electron microscope can be used to obtain information about the topography and the composition of a sample. The surface of the sample is scanned by a focused beam of electrons, which generates secondary electrons, backscattered electrons, X-rays, Auger electrons and cathodoluminescence [40].

Surfaces were imaged with an FEI MLA 650F scanning electron microscope (SEM) using secondary electron imaging (SEI) and backscattered electron (BSE) detection. Compositional data came from energy dispersive X-ray (EDX) detection on the same SEM. These three imaging modes are briefly introduced below.

2.5.1 Secondary electron detection

Secondary electrons are emitted from inner atom shells by inelastic excitations [41]. Normally, secondary electrons with energies less than 50 eV are collected by a detector. Therefore, the depth of the surface that secondary electrons emitted is only a few nanometers. However, a relatively high resolution (5–20 nm) can be reached [42]. In a secondary electron image, the brightness at different positions is related to the number of a secondary electron which the detector collected. If an electron beam is directed perpendicular to a flat surface, some of the secondary electrons won't emit from the surface because there is a small interaction volume. As the surface is more tilted or is more rough, more secondary electrons reach the detector, which results in a brighter image compared to a flat surface. Therefore, the difference of brightness is associated with the topography of the surface.

2.5.2 Backscattered electron detection

Backscattered electron (BSE) detection is based on the reflection of an electron beam from the sample by elastic scattering. The interaction volume for BSE is larger than for secondary electrons, and BSE can be generated from deeper positions within the sample. Moreover, the intensity of BSE is proportional to the atomic number of sample, which gives different atomic information within a BSE image [43]. In our research work, we used BSE to tell the difference between phases within our electrodeposited material. If the brightness of a BSE image is uniform, that means one phase dominate. If the brightness varied across a BSED image, this meant that multiple compositional phases existed in the electrodeposited sample.

2.5.3 Energy dispersive X-ray (EDX) detection

X-rays are generated when an electron from an inner shell is ionized and the electron from an outer shell fills to release energy. These characteristic X-rays are usually used for elemental analysis [40,43]. EDX, gave us another way to investigate the elemental composition of our electrodeposited surface, to compare with our BSED results.

2.6 Attenuated Total Reflectance Fourier transform infrared spectroscopy (ATR–FTIR)

Attenuated total reflectance (ATR) spectroscopy is associated with Fourier-transform infrared spectroscopy (FTIR) [44,45]. In this technique, an infrared beam travels into an ATR crystal with a certain angle. Then the infrared beam is reflected within the crystal several times while it is in tight contact with the sample. The reflection of the infrared beam induces an evanescent wave that penetrates into the sample. Normally, the penetration depth is between 0.5 and 5 micrometers. As a result, the molecules in the sample absorb energy from the evanescent wave based on the excitation energy of their vibrational modes. Then the attenuated evanescent wave is captured by the detector. Consequently, the characteristic absorption in the infrared region is recorded. The advantage of ATR-FTIR spectroscopy over classic FTIR spectroscopy is that each solid or liquid sample can be tested directly without any additional sample preparations.

In my research work, ATR–FTIR spectroscopy (Platinum ATR, Alpha, Bruker, shown in Figure 2.5) was used to characterize samples in Chapter 4. In Section 4.5, a deposit attached to the substrate was scraped to some fine white particles. Then particles were poured onto the crystal and pressed.

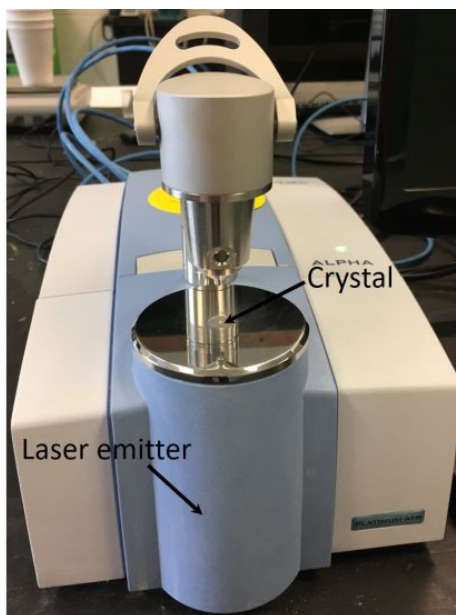


Figure 2.5: Photograph of ATR-FTIR spectrometer.

2.7 Profilometer measurements

Surface roughness was assessed with profilometer scans (Alpha-Step D-120 Stylus Profiler). The key component of our profilometer is a stylus with a 2-micron tip radius. The surface of the sample was scanned by the fine tip. This one-dimensional line of scanned surface generates a plot of height versus scan length. 1 mm lengths were scanned on the interest area of the sample with a $0.04 \mu\text{m}$ length associated with one data point. Moreover, the scan speed was set at 0.01 mm/s.

Chapter 3

Wettability studies of steel without electrodeposits

In this chapter, I described some basic treatments (chemical etching and organic coating). We attempted to fabricate a water repellent surface on carbon steel and stainless steel. Organic coatings (stearic acid, dodecanethiol, Aculon) were used to lower the surface energy. Chemical etching (hydrochloric acid, sulfuric acid, hydrogen peroxide) was used to increase the surface roughness. Static contact angle measurements were the main method to quantify the wettability.

3.1 Carbon steel substrate

A350 Gr Lf 2 Class 1 carbon steel bars (6 mm x 8 mm x 50 mm, obtained from Petroleum Research Newfoundland and Labrador) were prepared for organic coating and corrosion tests (Figure 3.1a). The chemical composition of A350 Gr Lf 2 Class 1 carbon steel includes $C \leq 0.020\%$, $Si \leq 0.8\%$, $Mn \sim 1\%$, $19.5\% \leq Cr \leq 20.5\%$, $6\% \leq Mo \leq 6.5\%$, $17.5\% \leq Ni \leq 18.5\%$, $0.5 \leq Cu \leq 1\%$ [46]. Prior to my experiments, the

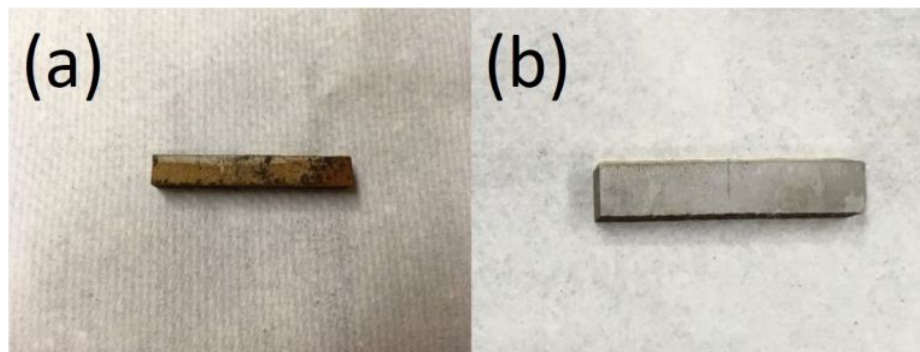


Figure 3.1: a: Photograph of rusted carbon steel. b: Photograph of clean carbon steel. Dimensions of the bars: 6 mm \times 8 mm \times 50 mm.

previously used carbon steel needed to be cleaned by immersing in 1 M HCl solution for 5 s to remove rust on the surface (Figure 3.1b).

3.1.1 Organic coating

Organic coatings have been widely used to create hydrophobic surfaces because of their low surface energies. In this section, three common organic coatings were studied: stearic acid (STA), dodecanethiol (DDT) and Aculon.

Stearic acid ($C_{17}H_{35}COOH$) is an 18 carbon chain saturated fatty acid. The polar group of stearic acid ($-COOH$) can be anchored with metal cations. As for the nonpolar group, the 18 carbon chain serves as the hydrophobic part. Stearic acid coating for hydrophobic surfaces has been investigated a lot. Some [47, 48] studied stearic acid coating on alumina and aluminum substrates with a simple immersion method, which dramatically increases the hydrophobicity of the surface. Others [49] introduced vapor deposition of stearic acid on a substrate.

Dodecanethiol can form a self-assembled monolayer whose head group, the thiol group, is an anchoring group on oxide-free metallic surface. Such self-assembled monolayers like DDT can be adsorbed on various surfaces [50]. In other research, coating DDT on bare silicon surfaces was discussed [51, 52]. Four hours of reaction duration

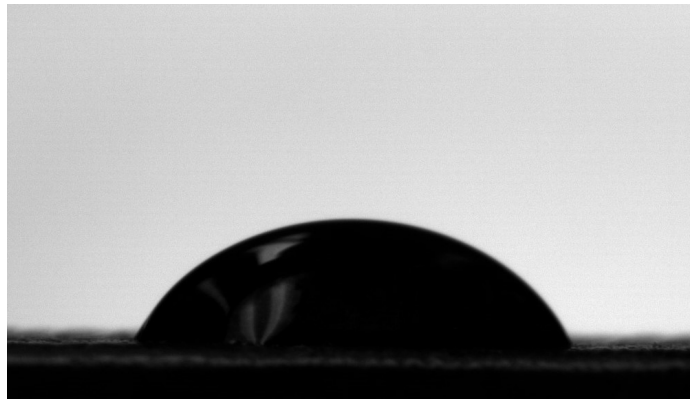


Figure 3.2: Photograph of a $5 \mu\text{L}$ water droplet on carbon steel. The contact angle here is 65° .

can make the water contact angle reach a maximum value. Higher ambient humidity can enhance the adhesion force between DDT and a silicon surface. Furthermore, coating DDT on other substrates such as Au nano-particles [53] and Cu meshes [54] has also been studied.

Aculon (Aculon Metal Repellency Treatment, San Diego, CA, USA) is a commercial hydrophobic coating [55]. It is a polymeric coating applied as an ethanol-based liquid. It is not widely reported in chemistry papers, but it is used in engineering applications.

The static contact angle is the most straightforward method to test the hydrophobicity of an organic coated surface. As mentioned in Chapter 2, six positions on the surface were randomly chosen to measure the static contact angle and the volume of each droplet was $5 \mu\text{L}$. For comparison, the hydrophobicity of the bare substrate was measured first. As shown in Figure 3.2, the static contact angle of bare carbon steel is $65 \pm 5^\circ$, which shows that the surface of bare carbon steel is hydrophilic.

3.1.2 Contact angle measurements

The sample preparation before contact angle measurements was slightly different for each organic coating.

Stearic acid: HCl-cleaned carbon steel was immersed in 0.05 M stearic acid solution (ethanol as solvent) for 50 min. Then the sample was dried in air.

Dodecanethiol: HCl-cleaned carbon steel was immersed in 1 M dodecanethiol solution for 240 min. Then the sample was withdrawn from the solution and rinsed with distilled water. After drying the sample in an oven (5 minutes at 50 degree Celsius), the contact angle was measured.

Aculon: HCl-cleaned carbon steel was immersed in the Aculon solution for 10 min and dried in air.

The wettability of dodecanethiol coated steel varies with the amount of time exposed to air. After the sample was withdrawn from the oven, the mean value of the contact angle increased to 92° (Figure 3.3a). However, after the sample was exposed to air for 24 h, the contact angle increased even more. The maximum value can reach 132° , as shown in Figure 3.3b. Thus, we chose the long exposure time (24 h) to compare with the other two organic coatings.

The mean static contact angle for different organic coatings is shown in Figure 3.4. It is obvious that the contact angle of all coated samples increased a lot compared to the contact angle of bare carbon steel. For a stearic acid coating, the contact angle is $131 \pm 6^\circ$. Although stearic acid serves as a coating to lower the surface energy, its nonuniform coverage on carbon steel surface triggers a large uncertainty ($\pm 6^\circ$). The reason that the coating is not uniform may be due to the heterogeneous elemental composition on the steel surface. Some parts of the carbon steel surface can form strong interactions with stearic acid; some parts do not. Dodecanethiol also enhanced the wettability, but a huge uncertainty ($\pm 10^\circ$) also reveals the heterogeneity of dode-

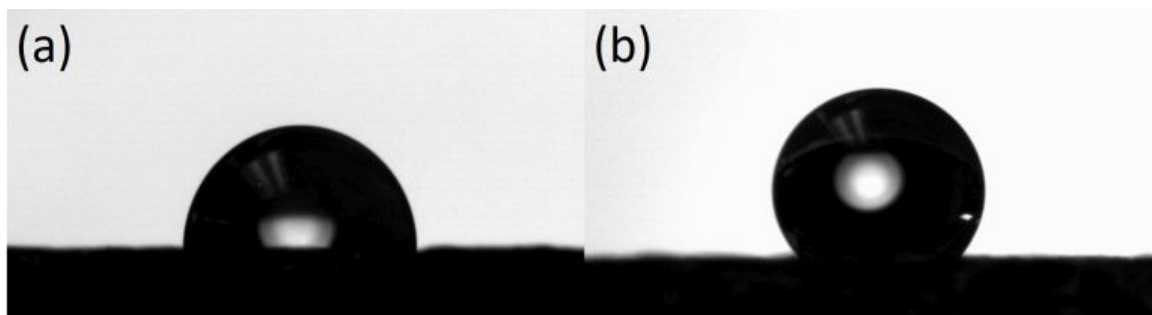


Figure 3.3: a: Photograph of a $5 \mu\text{L}$ water droplet on dodecanethiol coating. The contact angle here is 92° . b: Photograph of a $5 \mu\text{L}$ water droplet on 24 h exposed dodecanethiol coating. The contact angle here is 132° .

canethiol coverage. On a dodecanethiol coated surface, the maximum contact angle value is 132° , whereas the minimum value is just 104° . In comparison, the Aculon coating is more uniform than the others, with contact angles of $126 \pm 2^\circ$.

3.1.3 Polarization curves

Figure 3.5 shows the polarization curves of bare carbon steel and some organic coatings. The intersection point of each curve shows E_{corr} and j_{corr} . Based on the calculation from polarization curves, the corrosion parameters of all specimens are shown in Table 3.1. As mentioned above, higher corrosion potential and lower corrosion current indicates better corrosion resistance. As shown in Table 3.1, stearic acid and dodecanethiol indeed move E_{corr} more positive and have j_{corr} smaller compared to bare carbon steel, which means these two organic coatings enhance the corrosion resistance. There is no significant difference between dodecanethiol and stearic acid in terms of the corrosion resistance.

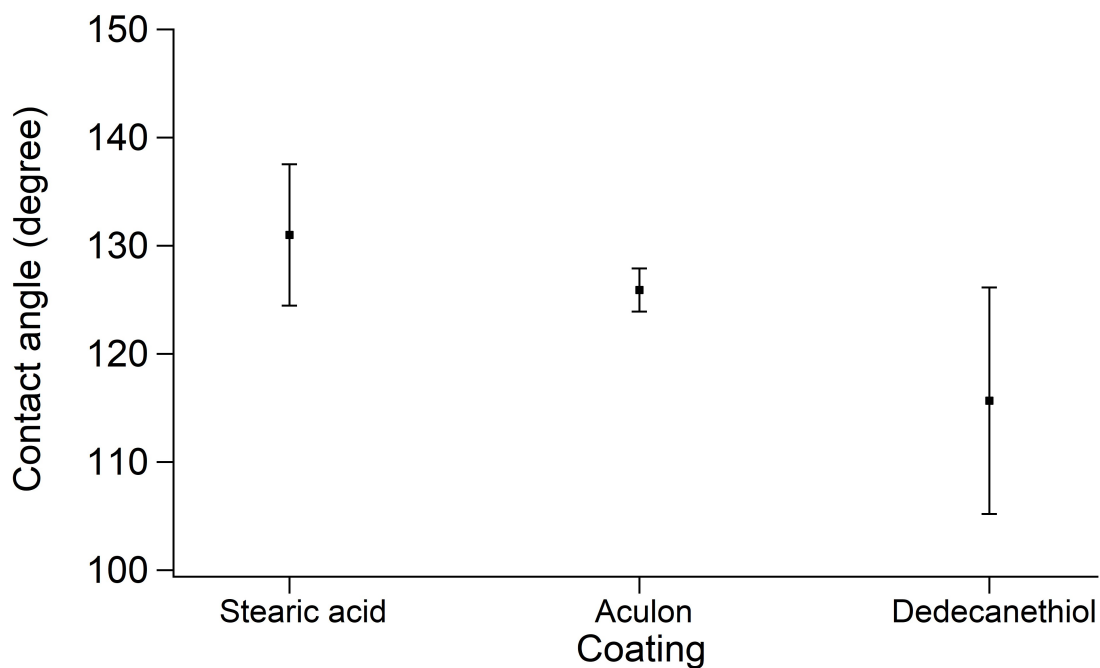


Figure 3.4: Static contact angle of three different organic coatings on carbon steel.

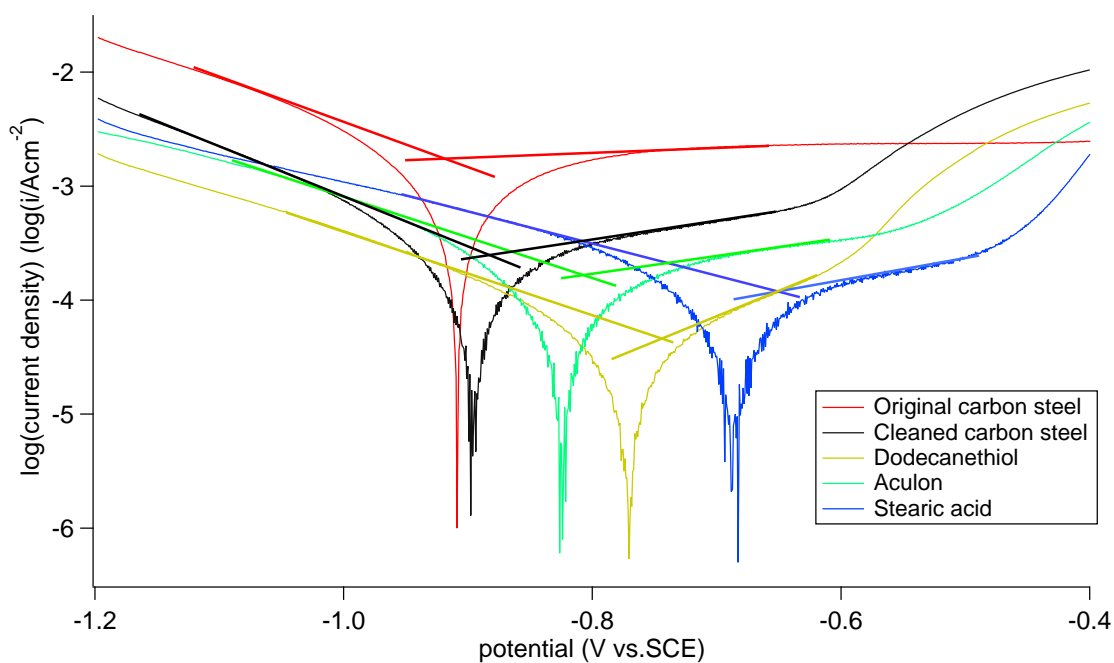


Figure 3.5: Polarization curves for different coating materials on carbon steel. The slope lines indicate the parts of the curves that were fit in order to extract E_{corr} and J_{corr} values.

Coatings	E_{corr} (V)	J_{corr} (A/cm ²)
Original carbon steel	-0.92 ±2%	$1.7 \times 10^{-3} \pm 3\%$
Cleaned carbon steel	-0.88 ±1%	$2.5 \times 10^{-4} \pm 2\%$
Dodecanethiol	-0.742 ±2%	$4.5 \times 10^{-5} \pm 1\%$
Aculon	-0.81 ±1%	$1.7 \times 10^{-4} \pm 3\%$
Stearic acid	-0.65 ±1%	$1.2 \times 10^{-4} \pm 2\%$

Table 3.1: Corrosion parameters for carbon steel with different organic coatings

3.2 Stainless steel substrates

In this section, the basic treatment and analysis of A403 – 6Mo stainless steel was studied. The chemical composition of A403 – 6Mo stainless steel includes C≤0.02%, Si≤0.8%, Mn~1%, 19.5%≤Cr≤20.5%, 6%≤Mo≤6.5%, 17.5%≤Ni≤18.5%, 0.5%≤Cu≤1% [56]. The stainless steel was cut into 6 mm x 8 mm x 50 mm stainless steel bars.

3.2.1 Chemical etching

Chemical etching is simple and can easily change the roughness of stainless steel. Based on others' work [57–59], we chose three different etching chemicals: H₂O₂, HCl and H₂SO₄. The concentration of each chemical was 1 M. The immersion time for each stainless steel bar was 2 min. As shown in Figure 3.6, the contact angle of bare stainless steel is $73 \pm 1^\circ$, which indicates a hydrophilic surface. With different chemical surface etching, the contact angle increases to various extents. For H₂SO₄ and HCl, the contact angle only increased to $92 \pm 2^\circ$ and $97 \pm 7^\circ$. Moreover, the contact angle of the HCl etched surface varies considerably with different positions. In comparison, the impact of H₂O₂ etching is more impressive with a contact angle of $115 \pm 1^\circ$.

Since chemical etching can increase the hydrophobicity of the surface, the combination of chemical etching and the organic coating was also studied, which means both of roughness and surface energy were modified. The combination of chemical etching and the organic coating has been studied by others [60,61]. Due to the high variabil-

ity of dodecanethiol coating on carbon steel, we did not study it in combination with chemical etching.

For stearic acid, three bare stainless steel samples were etched in other sulfuric acid, hydrochloric acid, and hydrogen peroxide as mentioned above. Then, etched samples were immersed in stearic acid (0.05 M) for 50 min. Comparing Figure 3.6 with Figure 3.7, the impact of the stearic acid coating is evident. The static contact angle of all samples increased overall due to the lower surface energy. As for the no etching sample and the sulfuric acid etched sample, the mean value of contact angles were $109 \pm 3^\circ$ and $108 \pm 2^\circ$, respectively, which means the etching by sulfuric acid didn't make any difference for the wettability. The positive impact of stearic acid coating on hydrochloric acid etched surface ($116 \pm 3^\circ$) and hydrogen peroxide etched surface ($130 \pm 3^\circ$) is not surprising.

For Aculon, three bare stainless steel were etched with other sulfuric acid, hydrochloric acid and hydrogen peroxide as mentioned above. Then etched samples were immersed in Aculon for 10 min. Just like stearic acid, Aculon can also increase the contact angle value compared to the bare chemical etched surface (Figure 3.8). For etched surfaces, the contact angle increases to $130 \pm 1^\circ$ (sulfuric acid), $126 \pm 2^\circ$ (hydrochloric acid) and $128 \pm 2^\circ$ (hydrogen peroxide). This demonstrates that the combination of roughness surface (chemical etching) and low surface energy surface (organic coating) contribute to a more water repellent material. However, none of these coatings can generate a low adhesion surface. Normally, a low adhesion surface can make a water droplet roll off with few degree tilting of substrate. For these samples, water droplets stick on the surface, even when the substrates were upside down. Given the undesirable high water adhesion of our coatings, there was no need to quantify the water repellency properties further.

3.2.2 Conclusion

In this chapter, both organic coating and chemical etching were applied to increase the hydrophobicity of steels. The experimental results show that all of the treatments can make surfaces more hydrophobic. However, the huge variability of static contact angle values reveals heterogeneous organic coverage and/or chemical etching. Among the organic coatings, Aculon worked best. Not only did it increase the static contact angle (126°), but it also had the lowest error bar ($\pm 2^\circ$). For chemical etching, hydrogen peroxide worked best. The static contact angle increased to $115 \pm 1^\circ$. We also tried to combine organic coating with chemical etching. As a result, the static contact angle increased even more. The maximum value was $130 \pm 1^\circ$. However, as mentioned above, no coating produced a low adhesion surface. This result did not meet our needs.

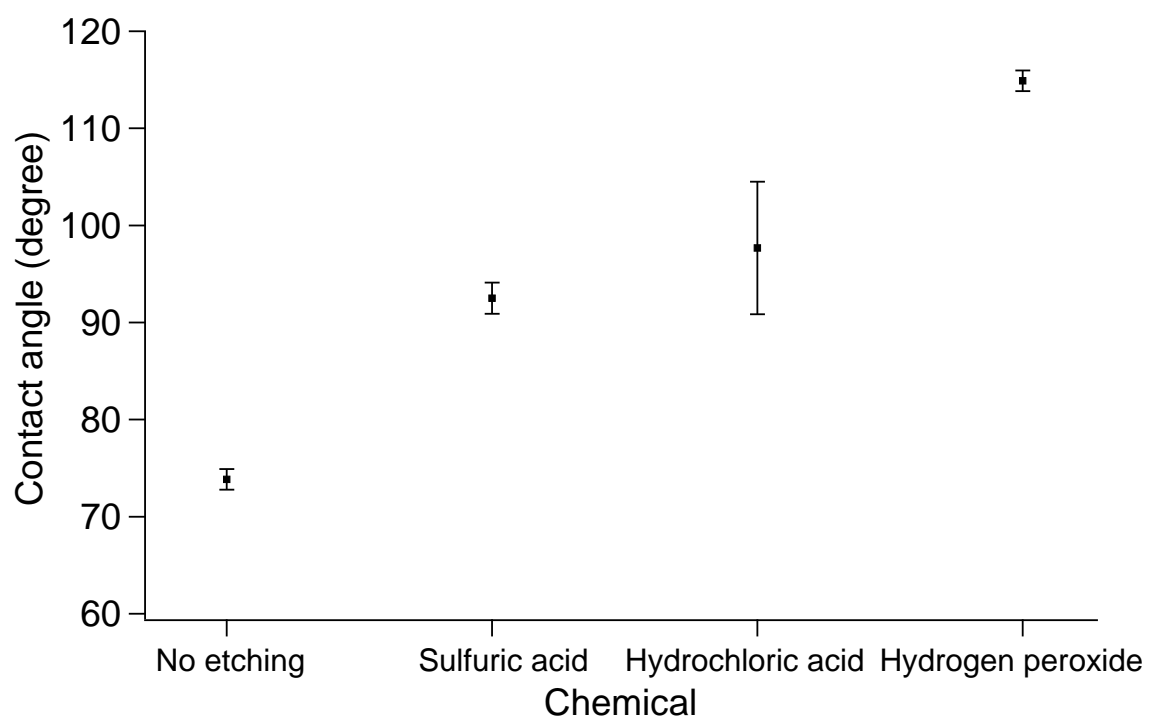


Figure 3.6: Static contact angles of 5 μL water droplets on bare stainless steel after different chemical etching treatments.

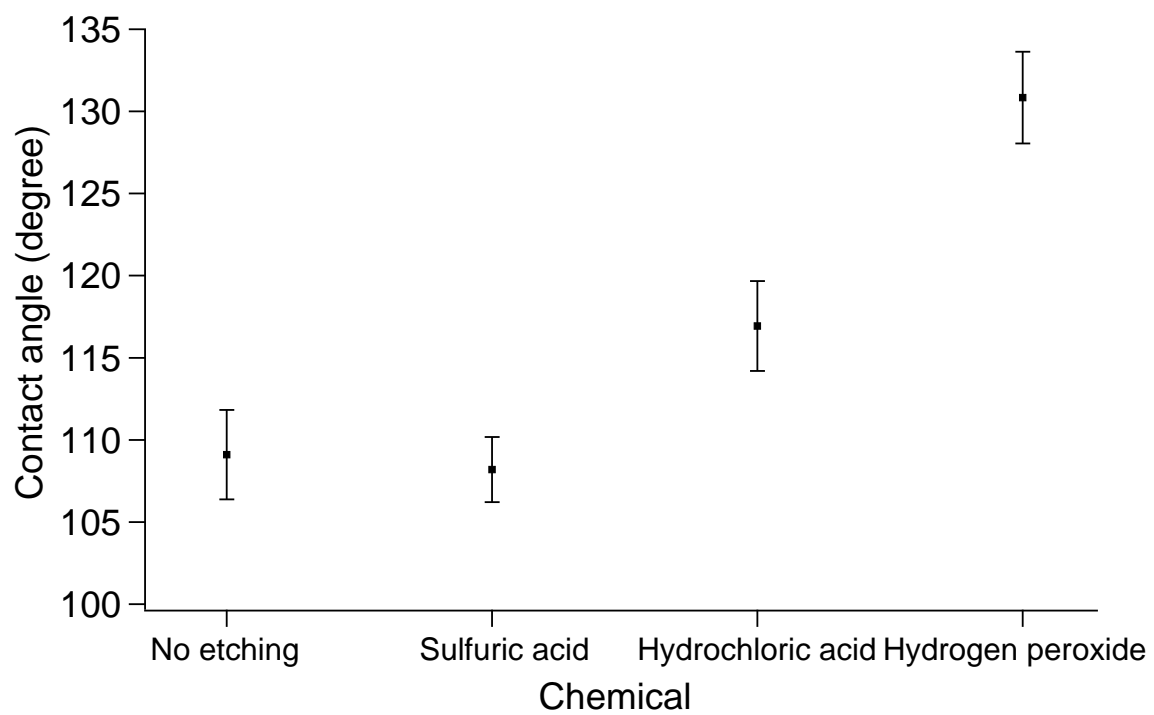


Figure 3.7: Static contact angles of 5 μL water droplets on stearic acid-coated stainless steel after different chemical etching treatments.

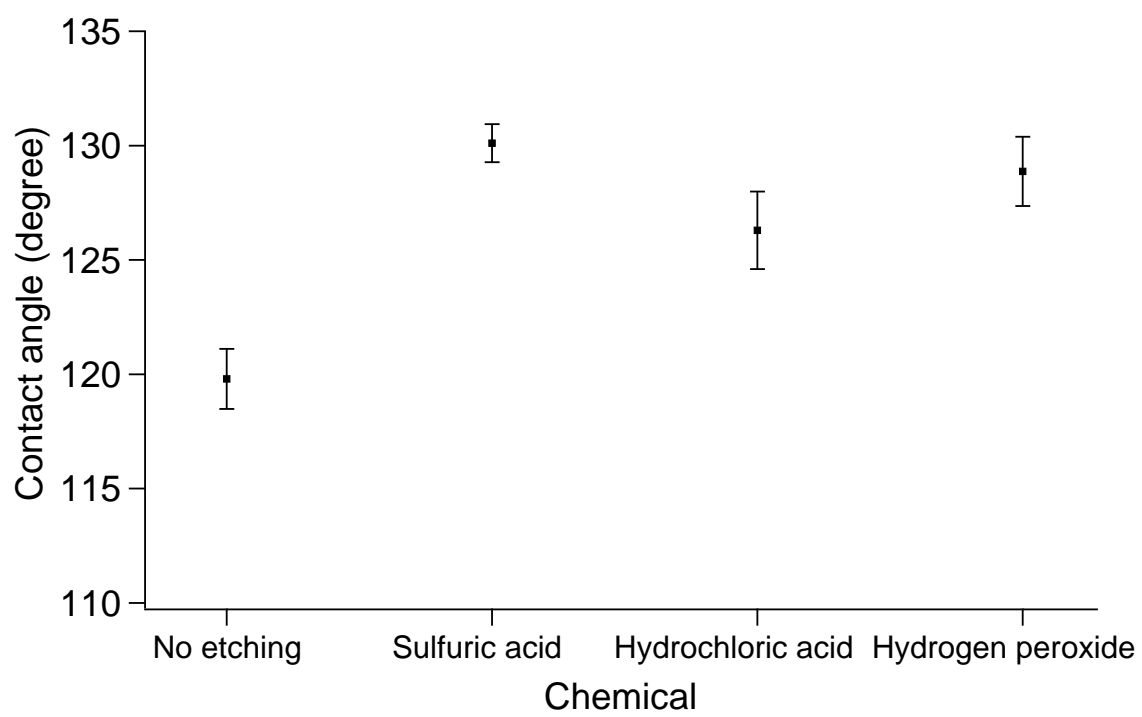


Figure 3.8: Static contact angles of 5 μL water droplets on Aculon-coated stainless steel after different chemical etching treatments.

Chapter 4

Zinc electrodeposition on carbon steel

Since chemical etching and organic coatings on our steel substrates did not produce a low adhesion surface, we sought another way to achieve this. In this chapter, electrodeposition of zinc will be described in detail. We detail our attempts to make a super-hydrophobic material on carbon steel by a combination of electrodeposited zinc, followed by the application of an organic coating. Contact angle measurements show that the most water-repellent surfaces are produced by using the combination of electrodeposition and an organic coating.

4.1 Zinc electrodeposition

Zinc has been widely used as a corrosion barrier to protect steel from corrosion in ambient environments [62, 63]. The composition of steel is mainly iron. In terms of electrochemistry, the standard reduction potential of zinc is more negative than iron, which means that zinc can be sacrificially oxidized in an ambient environment before

iron will.

Zinc deposits have been used to prepare superhydrophobic surfaces in recent years. For instance, a superhydrophobic surface can be formed by a combination of zinc deposits and polypropylene organic coatings [64]. There are many factors that vary in zinc electrodeposition, including morphology, size and compactness [29, 30, 65, 66]. Based on work by others [67], we chose the Zn-NH₄Cl-NH₃-H₂O system as our electrolyte for zinc deposition. For a wide region of pH values, multiple zinc complexes coexist in solution. But only one kind of zinc complex dominates at a specific pH value and specific potential. For instance, an amino-complex zinc (Zn(NH₃)₄²⁺) exists at alkaline pH values, whereas chloro- (ZnCl₄²⁻) plays a dominant role at low pH values. An acidic pH electrolyte is commonly used for zinc electrodeposition. Few reports talk about what deposits would be like if alkaline electrolytes were used. Although some [68–70] talked about the morphology of zinc crystals formed in an alkaline environment, none of them discuss their wettability. We investigated the hydrophobicity of zinc electrodeposits, prepared from an alkaline electrolyte based on Zn-NH₄Cl-NH₃-H₂O.

4.2 Zinc film deposition on carbon steel

Carbon steel bars (6 mm x 8 mm x 50 mm) were prepared as substrates (working electrodes). The electrodeposition area of the working electrode was 1 cm². The counter electrode was a carbon rod that matched the area of the working electrode. The general procedure for electrolyte preparation and electrodeposition is described in Section 2.1. Here, we used a current density of 30 mA/cm² for a deposition time of 30 min.

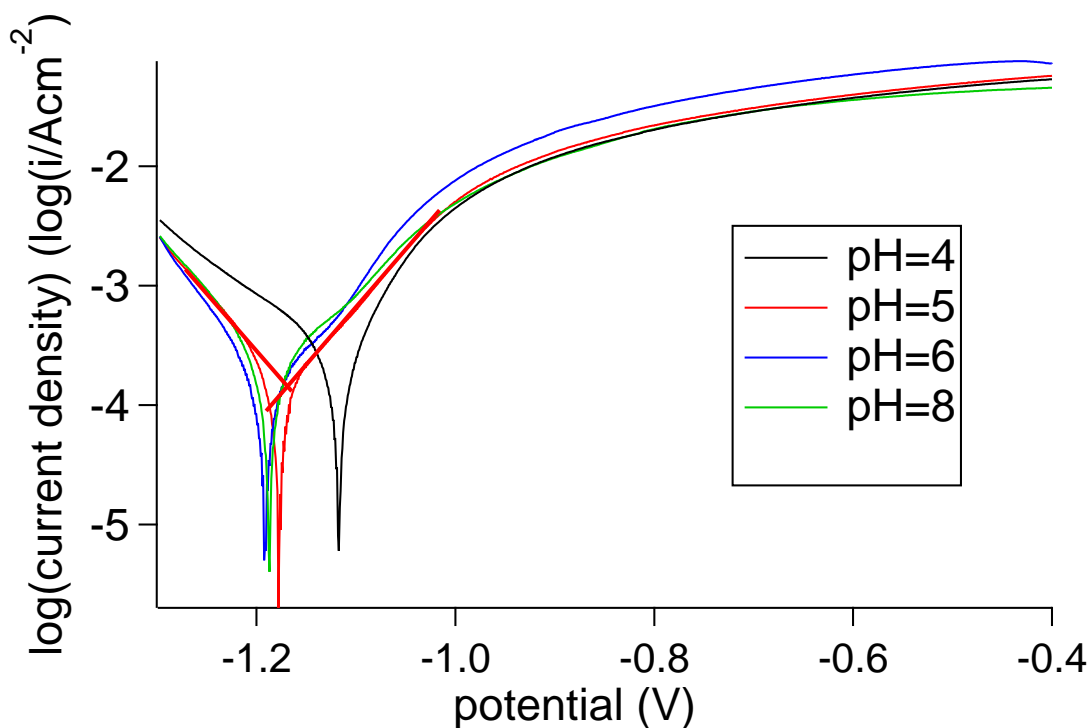


Figure 4.1: Polarization curves for zinc electrodeposits prepared at different pH values.

4.2.1 Polarization curves

Polarization curves were used to measure the corrosion resistance of zinc deposits synthesized at different pH values. What we look for in the plots (Figure 4.1 is the corrosion potential (E_{corr}) and corrosion current density (j_{corr}). Figure 4.1 shows the polarization curves for different zinc coatings. E_{corr} and j_{corr} are obtained by following the linear regions of each cathodic and anodic reaction. The intersection point the cathodic line and anodic line is j_{corr} and E_{corr} . Normally, higher E_{corr} and lower j_{corr} reflects better corrosion resistance. As shown in Table 4.1, E_{corr} and j_{corr} are similar for pH 5,6,8. When the pH value is 4, the exponential curve moves more positive along the horizontal axis (Figure 4.1), which means the E_{corr} is slightly higher. But overall, there is no big difference in terms of E_{corr} and j_{corr} between deposits prepared at different pH values.

Zinc Coatings	E_{corr} (V)	J_{corr} (A/cm ²)
pH=4	-1.1 ±2%	$2.7 \times 10^{-4} \pm 3\%$
pH=5	-1.2 ±1%	$1.3 \times 10^{-4} \pm 1\%$
pH=6	-1.2 ±3%	$1.5 \times 10^{-4} \pm 1\%$
pH=8	-1.2 ±2%	$1.5 \times 10^{-4} \pm 2\%$

Table 4.1: Corrosion parameters of different zinc coatings

4.2.2 Dodecanethiol (DDT) coatings

After zinc was electrodeposited, the sample was rinsed with water and dried in air. The hydrophobic coating was applied by simply immersing the sample in a dodecanethiol solution (1M) for 240 min. By coating with dodecanethiol, the contact angle increases compared to the contact angle for dodecanethiol-coated steel. The coverage on zinc is more uniform than the coverage on bare carbon steel, which can be seen in the smaller error bars on the static contact angles. According to Section 3.1.1, the contact angle of DDT coated carbon steel was $115 \pm 10^\circ$ (Figure 3.4). For DDT on zinc electrodeposits, the static contact angle was $130 \pm 3^\circ$. Figure 4.2 shows representative photos of the maximum contact angle ($134 \pm 2^\circ$) and minimum contact angle ($128 \pm 1^\circ$) obtained for DDT-coated zinc. The uniform coating of DDT on zinc is not surprising. Others [71] discussed the remarkable adhesion between organothiol head-groups and oxide-free zinc. However, the droplets still pin easily on those surfaces, which means the water-repellency of this surface didn't meet our expectations.

4.2.3 Stearic acid coatings

Stearic acid coatings on zinc were also investigated. For the organic coating procedure, the only difference compared to DDT is that the immersion time of stearic acid coating (0.05 M) was 50 min. This procedure produces a very remarkable hydrophobic surface. It's hard to measure the static contact angle of this surface using a 5 μ L droplet. Because of the low surface adhesion, these small droplets were not pinned on the

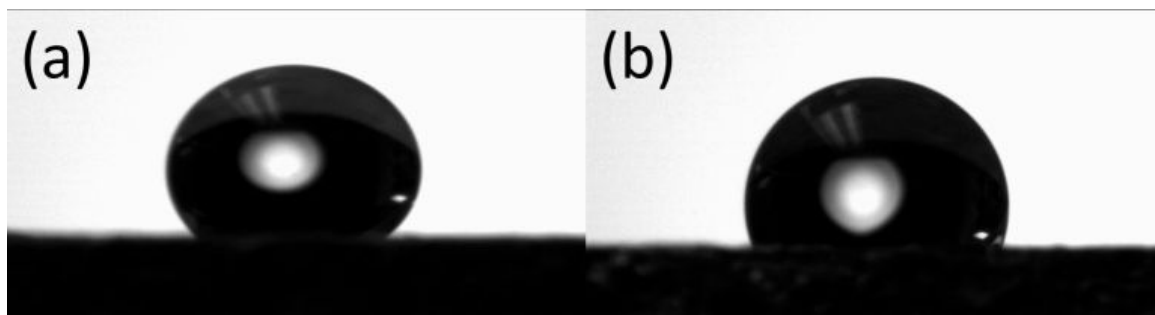


Figure 4.2: These representative photos show water droplets on dodecanethiol coated zinc surfaces. a: maximum contact angle value ($134\pm 2^\circ$), and b: minimum contact angle value ($128\pm 1^\circ$).

surface, but remained on the needle when the needle was withdrawn. Therefore, a larger volume ($20\ \mu\text{L}$) was used to measure the static contact angle. The larger weight of the big droplet caused the water droplet to stick on the surface instead of remaining stuck to the needle. The static contact angle of this surface was $150\pm 2^\circ$. However, the zinc film did not totally cover the surface. As shown in Figure 4.3, there are some white dots on the surface. During the contact angle measurement, we also found that large droplets did not stick to their original positions. Instead, droplets would slide to the positions of white dots and stick there. We think the reason that larger water droplets can stick on the surface is that they touch more easily the white areas where the droplet can be easily pinned. A pinned water droplet may have a large difference between the left contact angle and the right contact angle. Young's equation (Equation 1.2) does not account for this observation.

The appearance of white dots may be due to the lack of zinc coverage. Even so, the poor adhesion of water to this surface in other areas is still impressive. With only 3° tilting of the sample, a droplet can roll off from the surface (Figure 4.4).

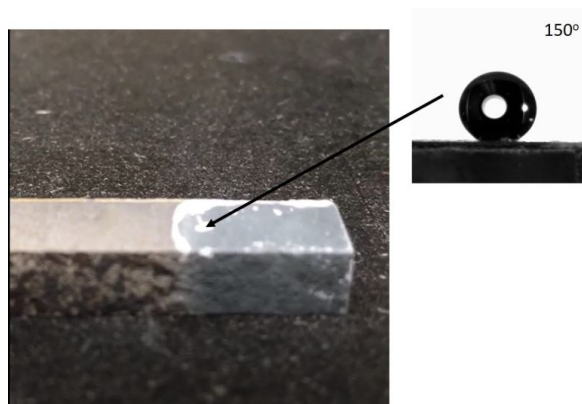


Figure 4.3: Photograph of stearic acid coated zinc film on carbon steel, and an image of a $5 \mu\text{L}$ water droplet on the surface.

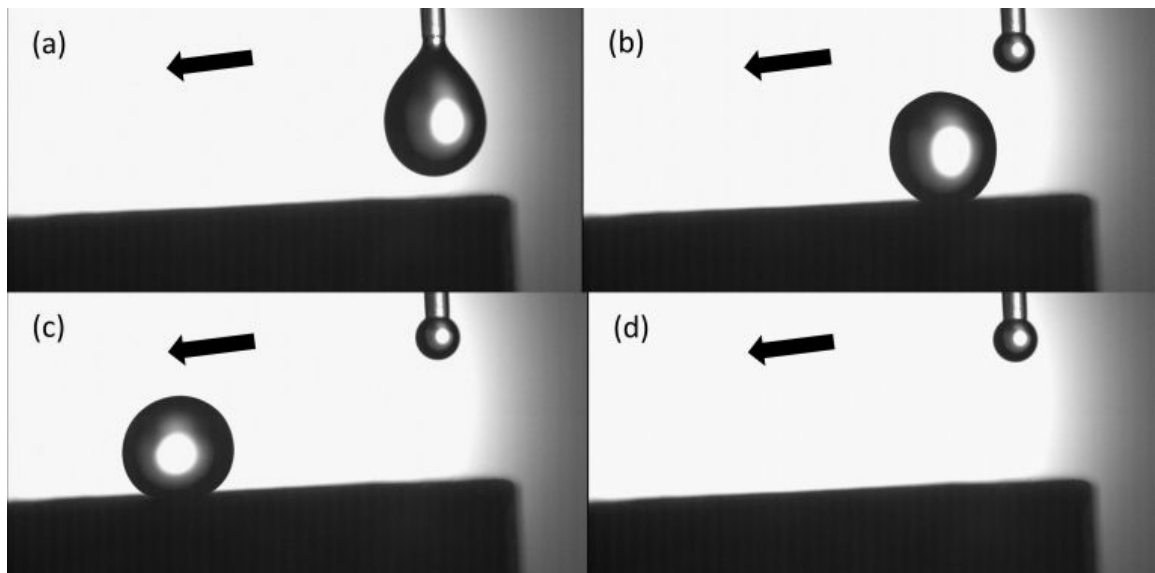


Figure 4.4: A series of snapshots of a water droplet rolling off the surface of a galvanostatically produced zinc film with stearic acid coating.

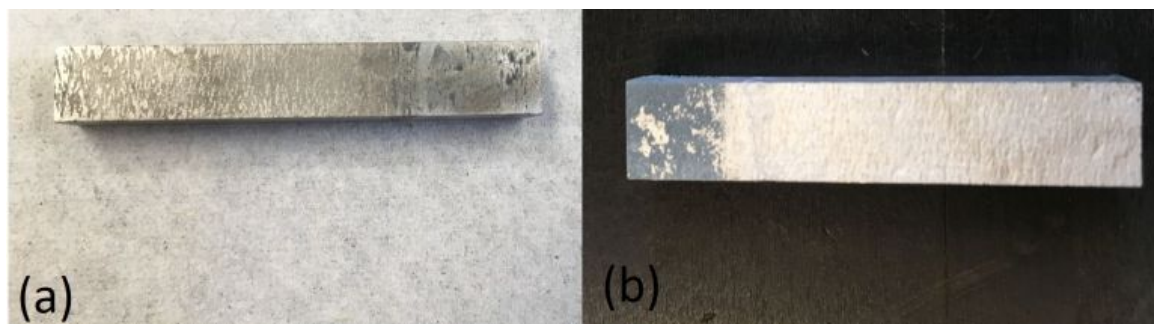


Figure 4.5: Photograph of a: no zinc layer on stainless steel, and b: zinc deposit that is partially rinsed off of the stainless steel. Dimensions of the bars: 6 mm \times 8 mm \times 50 mm.

4.3 Zinc deposition on stainless steel bars

Since the zinc film with stearic acid coating generates such impressive hydrophobicity, we investigated if this procedure could also be applied to stainless steel. Stainless steel bars (6 mm \times 8 mm \times 50 mm) were used as substrates and the electrodeposit area was 1 cm². The same synthesis procedure for zinc electrodeposition was used: constant current of 30 mA/cm² for 30 min. However, a zinc film failed to form on the substrate (Figure 4.5a). Even when the zinc film appeared occasionally, the deposit was loose and easily rinsed off (Figure 4.5b).

4.3.1 Modification of the zinc electrodeposition procedure

Based on the experience accumulated from galvanostatic (30 mA/cm²) zinc electrodeposition on carbon steel, we knew that the potential between the working electrode and reference electrode was near -1.3 V vs SCE. Therefore, we switched from galvanostatic to potentiostatic deposition at -1.3 V. As a result, the zinc electrodeposit was uniform (Figure 4.6). The current density was controlled by adjusting the distance between the working electrode and reference electrode while applying the constant potential due to the change in uncompensated resistance. We found 50 mA/cm² is

the optimized current density for uniform zinc coverage.

After zinc electrodeposition, the organic coating also needed to be optimized. Previously, the sample was immersed in 0.05 M stearic acid for 50 min. This procedure is time consuming and sometimes the surface was not hydrophobic enough after the stearic acid coating. Based on multiple trials, 5 min immersion time was enough for stearic acid coating. In addition, right after zinc electrodeposition, it helped to dry the sample in an oven at 50 °C for 3 min. The reason we accelerated the evaporation of water in the oven instead of drying the sample in air is because the zinc deposit was easily oxidized in the ambient. We needed to minimize oxidization. After the modifications mentioned above, a uniform zinc coating formed and the adhesion was excellent. The consecutive photos in Figure 4.7 show the poor adhesion of water to the surface. A droplet could roll off the surface without a significant angle of inclination.

To quantify the water adhesion to a surface, contact angle hysteresis is a common measurement. Contact angle hysteresis can be measured using a dynamic sessile drop method, which tracks the advancing contact angle and receding contact angle by expanding and shrinking the volume of a water droplet, without increasing the solid–liquid interfacial area. however a prerequisite of this method is that the droplet will stay on the surface so that the needle tip can be inserted (to change the volume of water). For our zinc-coated samples, water droplet could not stay on the surface. Moreover, when we tried to insert the needle tip into the center of droplet, the droplet slide to the other side. Thus, it was hard for us to quantify the adhesion. Because it was impressively low.

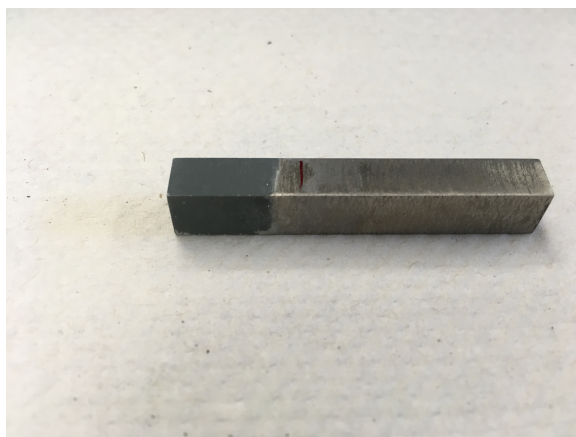


Figure 4.6: Photograph of a uniform zinc film on a stainless steel bar. Dimensions of the bar: 6 mm \times 8 mm \times 50 mm.

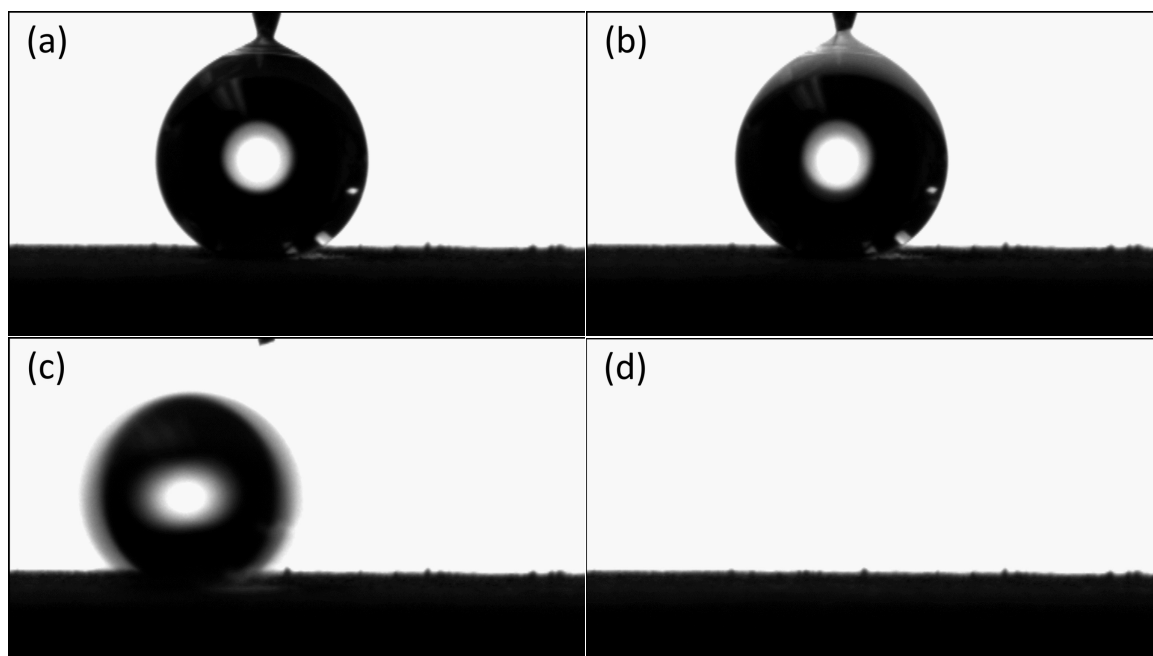


Figure 4.7: A series of snapshots of a water droplet rolling off a potentiostatically produced zinc electrodeposit with stearic acid coating on stainless steel substrate.

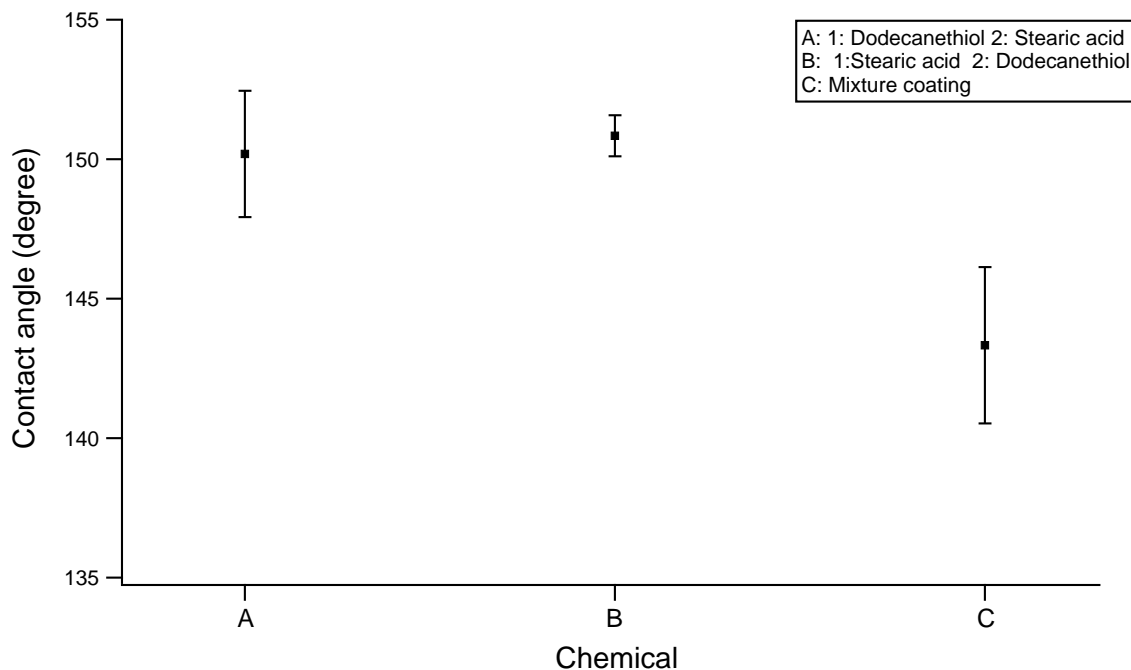


Figure 4.8: Static contact angles of 5 μL water droplets on zinc films with different organic coatings.

4.4 Mixtures of organic coatings

Since zinc electrodeposits with a stearic acid coating show impressive low water adhesion, we investigated if a mixture of organic coatings could change the wettability. As shown in Figure 4.8, for coating A, the electrodeposit was immersed in dodecanethiol for 2 h, then stearic acid for 15 min. Coating B had stearic acid (15 min) first, followed by dodecanethiol (2 h). Coating C had a mixture of stearic acid and dodecanethiol (v:v=1:1, 1M). Based on 5 different positions of water droplet measurements, the static contact angles of coatings A and B reached $150 \pm 2^\circ$ and $151 \pm 1^\circ$, respectively. However, the adhesion was still strong, with droplets readily pinning at many positions on the surface. The contact angle for coating C was slightly worse ($143 \pm 3^\circ$) and water droplets still pinned easily. In these cases, the mixture of organic coatings was not more helpful than a pure stearic acid coating.

4.5 ATR–FTIR analyses

During zinc electrodeposition, we found a white layer formed on the surface before the appearance of a gray zinc film. We used ATR–FTIR to characterize the white material. As shown in Figure 4.9, there are some evident peaks (3000 cm^{-1} and 1650 cm^{-1}). Based on FTIR databases [72], we found these peaks could be related to stretching modes and bending modes of N–H. The existence of N–H is reasonable since a high concentration of NH_4Cl is utilized in the electrolyte. Moreover, the peaks around $1372\text{--}1290\text{ cm}^{-1}$ could be related to a stretching mode of N–O. ATR–FTIR alone cannot totally explain the composition of this electrodeposit. ATR–FTIR cannot detect pure Zn since it detects energies that are characteristic of the vibration mode of covalent bond, not metallic bonds. The vibration of other zinc compounds, such as ZnO [73], can be detected by FTIR, but we did not observe them. To detect pure Zn, future studies could use XRD for the phase identification of crystalline material. In addition, chemical analyses such as ICP–MS would provide useful atomic composition information.

ATR–FTIR is a potential method to characterize *in situ* large area wetting [74,75]. We did some preliminary characterizations and tried to find the relation between the intensity of O–H vibrations and the hydrophobicity of surfaces. We didn't get meaningful data from this characterization, so it is not described in detail here.

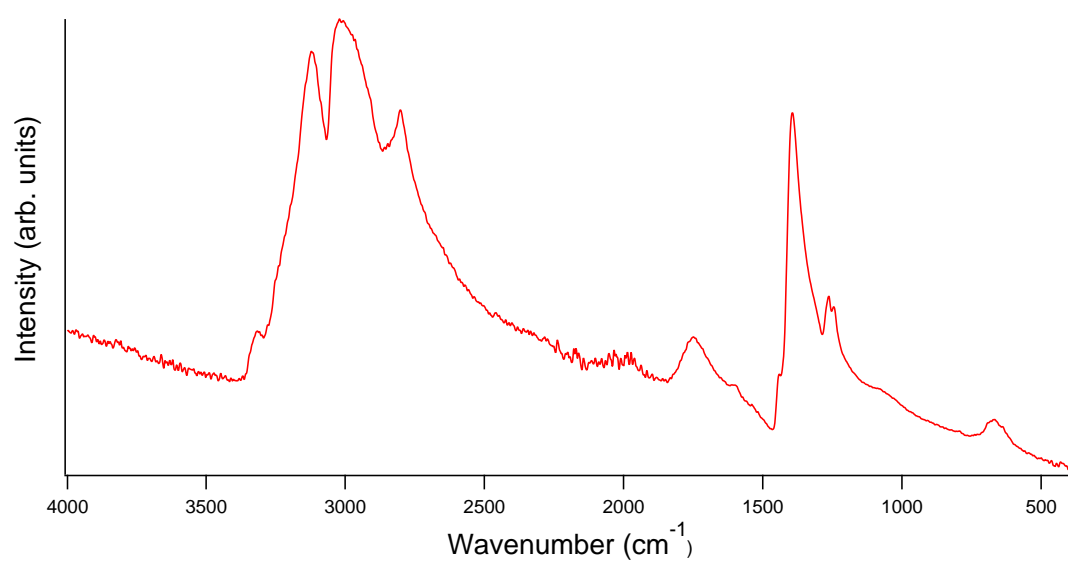


Figure 4.9: ATR-FTIR of white deposits scraped from the stainless steel substrate during early stages of zinc electrodeposition. Peaks are likely related to N-H and N-O species.

Chapter 5

Zinc electrodeposits for water repellent surfaces

This chapter is published in the Journal of The Electrochemical Society [76]. The authors of this paper are Boyang Gao and Dr. Kristin Poduska. Boyang Gao carried out the experiments, data analysis and contributed to the writing of the manuscript. Dr. Kristin Poduska provided guidance over the experimental design, data analysis, and the writing of the manuscript.

5.1 Introduction

Controlling the way that water wets a surface is a very popular research subject because it affects how durable the material will be against factors such as corrosion, ice accretion [77, 78], and fouling [79]. To reduce wetting of static water droplets, there are general guidelines and simple models that demonstrate this can be achieved with combinations of micron-scale and nanometer-scale surface roughness, in addition to a low surface energy. [22, 80, 81] This produces air pockets between water droplets

and the surface, leading to superhydrophobicity with a very high apparent static contact angle. However, droplets that do not wet a superhydrophobic surface well can still adhere strongly, which makes them hard to remove even if the surface is tilted. It is still an open research question to model and predict exactly what structural characteristics prevent water droplets from adhering to a surface because this varies with droplet size, and it is also affected by topographic asperities on the surface. [82–84] For industrial structural materials such as stainless steel, reducing droplet adhesion is very desirable, but it is particularly difficult because of their innately high surface energy, multi-component chemical compositions, and complex surface shapes. Thus, it is a challenging and interesting research question to control both wettability and water adhesion on stainless steel.

Many groups have roughened stainless steel surfaces to improve their water repellent properties, using either removal strategies (such as chemical etching [57–59, 61] and sandblasting [60, 85, 86]) or additive strategies (such as thermal evaporation [87], sol-gel, [88] and electrodeposited layers [25, 29, 64, 71]). Electrodeposits change the surface topography, and some studies have checked to see if this correlates with changes in static contact angles. [25, 29, 64] Adding surfactants to electrolytes is another strategy to control crystallite nucleation and growth. Such additives can alter the evolution and adsorption of hydrogen gas, and they can also passivate specific crystallite faces to alter crystallite morphologies. In the case of Zn, electrodeposition tends to produce dendritic crystallites where current distributions are not uniform, so additives are often beneficial. [67, 89–91] Zn and Zn-alloy electrodeposition has been widely used as a corrosion protection barrier on steel. [64, 71]

In this work, we demonstrate that a mildly alkaline electrolyte (pH=8) that contains a surfactant (polyethyleneimine, PEI) can be used to produce Zn electrodeposits that have very low adhesion for macroscopic water droplets. We discuss the range

of deposition parameters (electrolyte composition, pH, applied potential, and coating procedures) that produce the best water-repellent surfaces.

5.2 Experimental

5.2.1 Electrodeposition

Electrolytes contained 0.2 M ZnCl_2 (ACS grade, 97.0%, Caledon) and 3.5 M NH_4Cl (ACS grade, 99.5%, ACP) in ultrapure water (Barnstead, $18.2 \text{ M}\Omega\cdot\text{cm}$). We note that a large amount of white precipitate formed initially, but the solution cleared once the pH increased above 7.5 by adding NaOH (ACS grade, 97.0%, ACP). In this study, we used electrolytes with pH values between 7.5 and 8.5. After setting the desired pH, 100 ppm polyethyleneimine (PEI), a variable mass polymer with a repeat unit mass of 42.03 amu, was added as a surfactant.

Electrodeposits were prepared on high-strength, precipitation-hardened stainless steel (SAE 630/ 17-4, 1 mm thickness, McMaster-Carr) that is rich in Cr, Ni, and Cu. The 3 cm \times 3 cm working electrodes were cleaned by sonication in ethanol (15 min, 95%, Commercial Alcohols, Inc.), then ultrapure water (15 min, $18.2 \text{ M}\Omega\cdot\text{cm}$, Barnstead), then drying in air at ambient temperature. The counter electrode was carbon felt (99.0%, Alfa Aesar), and all deposition potentials are reported relative to a saturated calomel (SCE) reference. Deposition was carried out at constant potential (-1.3 to -1.5 V *vs.* SCE) for 15 min at room temperature while stirring at 200 rpm. During the electrodeposition process, the current density typically decreased from $-0.2 \text{ A}/\text{cm}^2$ to $-0.15 \text{ A}/\text{cm}^2$. Afterwards, the sample was rinsed with ethanol and immediately immersed in an ethanol-based solution of 0.05 M stearic acid (95.0%, Sigma-Aldrich) for 5 min, then rinsed with ethanol and air-dried. For comparison, other samples were rinsed with ultrapure water (instead of ethanol) and allowed to

air-dry before immersion in the stearic acid solution.

5.2.2 Characterization

X-ray diffraction (XRD) data were collected with a Rigaku Ultima-IV (Cu $K\alpha$, $\lambda = 1.54059 \text{ \AA}$) over a range of $5\text{-}90^\circ 2\theta$ with 0.02° step size. Lattice constant refinements were facilitated with Jade software (Materials Data Inc.). Surfaces were imaged with an FEI MLA 650F scanning electron microscope (SEM) using secondary electron imaging (SEI) and backscattered electron (BSE) detection. Compositional data came from energy dispersive x-ray (EDX) detection on the same SEM. Surface roughness was assessed with profilometer scans (Alpha-Step D-120 Stylus Profiler) over 1 mm lengths with a $0.04 \mu\text{m}$ step size. Water droplet adhesion and static contact angles were assessed using droplets with $5 \mu\text{L}$ volume (Dataphysics OCA 15EC contact angle instrument).

5.3 Results and Discussion

We analyzed the structure, composition and crystallite morphologies of the resulting electrodeposits, as well as their water repellency properties. Representative XRD data (Figure 5.1) for electrodeposits with optimized water repellency (produced at $\text{pH} = 8$, $E = -1.5 \text{ V}$) show eight peaks that are consistent with hexagonal Zn ($P6_3/mmc$ (194), JCPDS card 98-000-0482 with $a = 2.6650 \text{ \AA}$, $c = 4.9470 \text{ \AA}$). [92] The remainder of the peaks are associated with either the stainless steel substrate (*) or the stearic acid overcoat (+).

Even though XRD data indicate that the electrodeposits are pure Zn with no preferred orientation, SEM images show a mix of crystallite morphologies and orientations (Figure 5.6a). The majority of the deposit is composed of micron-scale blocky

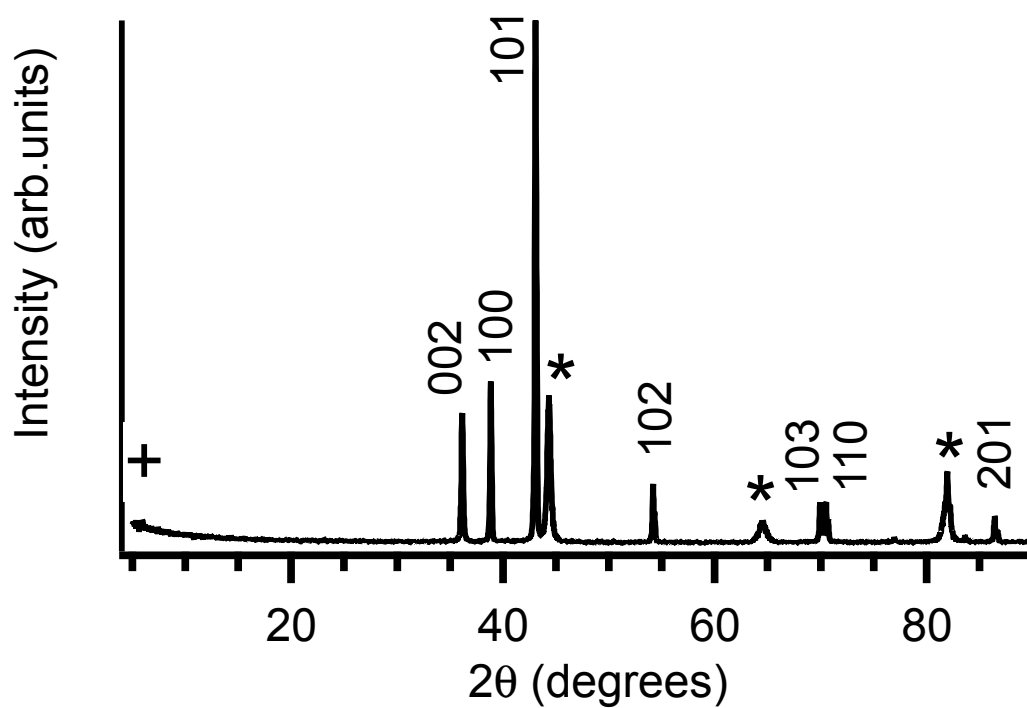


Figure 5.1: Representative XRD data for a Zn electrodeposit prepared at optimized deposition conditions ($\text{pH} = 8$, $E = -1.5 \text{ V}$) and then coated with stearic acid. The hkl indices correspond to the unit cell for hexagonal Zn (JCPDS 98-000-0482), asterisk (*) denotes peaks due to the stainless steel substrate, and plus (+) denotes a peak related to stearic acid.

crystallites, and there are also needle-shaped and hexagonal plate habits interspersed over a scale of tens of micrometers.

5.3.1 Use of surfactant

The crystallite morphology and substrate coverage of electrodeposited Zn has been widely studied, and the effects of additives – including complexing agents and surfactants – are widely reported. Because of its hexagonal crystal structure, the two most common crystal habits for Zn are plates or rods (needles). [65] As is typical for metal deposition, acidic pH values are commonly used for Zn electrodeposition. There are comparatively few reports that investigate Zn metal deposition from mildly alkaline electrolytes. Reports show that Zn electrodeposition based on ZnO and KOH as alkaline electrolytes also yields needle-shaped crystallites. [90,91] Using cetyltrimethylammonium bromide in the electrolyte suppresses dendritic growth and produces a higher density of small spherical crystallites. [91] Other additives such as PEI can change the morphology of dendrite tips from sharp to round.

In our experiments, Zn-based electrolytes without PEI surfactant had macroscopic variations in coverage and deposit color, and this was correlated with areas where hydrogen gas bubbles formed on the substrate during deposition. In areas of incomplete film coverage, water droplets adhered strongly to the surface and were easily pinned. SEM images show that the absence of PEI had a dramatic effect on the crystal habit of the Zn crystallites. Figure 5.2b shows blocky hexagonal crystals that are an order of magnitude larger than those produced from electrolytes that do contain PEI. In addition, there are gaps between individual crystallites that are tens of micrometers in size. For these reasons, we opted to use PEI in all of our electrolytes. We note that there was no evidence of PEI incorporation into the electrodeposits, based on XRD data.

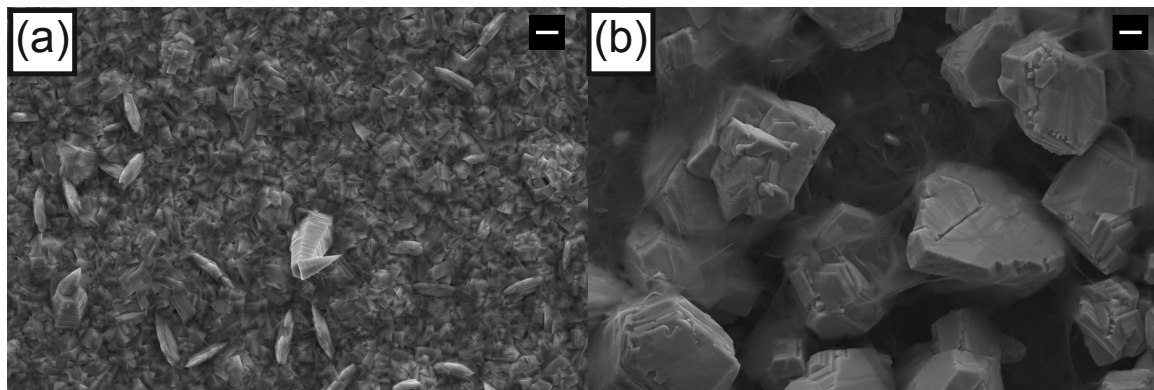


Figure 5.2: Representative SEM images of Zn electrodeposits (a) with PEI surfactant and (b) without surfactant. Scale bars for both images are $2 \mu\text{m}$, and both samples were prepared at -1.5 V and $\text{pH} = 8$.

5.3.2 Variation of pH and deposition potential

In general, Pourbaix diagrams are a helpful tool for optimizing electrodeposition conditions because they identify the pH and potential regions that will give a desired electrodeposit composition. We based our electrolyte on calculated Pourbaix diagrams for the $\text{Zn-NH}_4\text{Cl-NH}_3\text{-H}_2\text{O}$ system, [67] but with the addition of PEI surfactant. The useful pH and potential range we found for Zn deposition was consistent with the calculated Pourbaix diagrams.

In ammonium- and chloride-containing electrolytes, the kinds of Zn-based solution complexes vary considerably as a function of pH, especially near neutral pH. [67] $\text{ZnNH}_3\text{Cl}_3^-$ dominates when pH is between 7 to 7.4, while $\text{Zn}(\text{NH}_3)_3\text{Cl}^+$ forms when the pH ranges from 7.4 to 7.8. When pH sits between 7.8 and 12.5, $\text{Zn}(\text{NH}_3)_4^{2+}$ is the primary complex. In our experiments, white precipitates formed when the pH value was near 7, but disappeared once the pH increased above 7.5. As the alkalinity of the electrolyte increased, more negative deposition potentials were required to trigger Zn deposition, which caused more hydrogen gas bubbles to appear on the sample during deposition, resulting in incomplete deposit coverage. Therefore, we determined that

mildly alkaline electrolytes (7.5-8.5) were optimal for our purposes. Adjusting the electrolyte pH over this small range had an effect on the electrodeposit topography. As shown in Figure 5.6a-c, there are more large needle-shaped crystallites at higher pH values, when using the same deposition potential ($E = -1.5$ V).

We also investigated the effects of changing deposition potential between -1.0 V to -1.5 V, in steps of 0.1 V. At deposition potentials more positive than -1.3 V, no deposit formed. At -1.3 V, the Zn crystallites are sub- μm particles without clear facets. At -1.4 V, there are μm -sized overlapping hexagonal crystallites. At -1.5 V, needles and large blocky agglomerates appear at the expense of the overlapping hexagonal crystallites. Therefore, more negative deposition potentials give rise to larger sizes and more variety in the Zn electrodeposit morphologies. Representative SEM images over the range of potential and pH conditions are shown in Figure 5.6d-f.

Given that there are so many changes in the surface topography of the electrodeposit induced by different electrolyte pH and deposition potentials, it is worthy of note that there was a correlation between the electrodeposition conditions and the resulting water repellency. In all cases described above (pH between 7.5 and 8.5, E between -1.3 V and -1.5 V), there are significant portions of the 9 cm^2 sample on which water droplets do not adhere. The best deposition conditions were pH values of 8.0-8.5 using a deposition potential of -1.5 V. With these optimized parameters, the entire 9 cm^2 surface was routinely free of droplet pinning sites, except for the few mm around the deposit edges. We note that, for these experiments, the distance between the WE and CE was 4 cm, and this yielded a current density near 0.033 A/cm^{-2} . A closer electrode spacing (3 cm), increased the current density (0.045 A/cm^{-2}), but did not show an appreciable change in droplet pinning.

5.3.3 Protection from water and oxidation

A stearic acid overlayer plays a key role in preserving the integrity of the Zn electrodeposits. As mentioned in the Experimental description above, the electrodeposit must be rinsed with ethanol and immersed in the stearic acid immediately. When this capping layer is added, the electrodeposits retain their poor water-adhesion behaviours for many months. This is not surprising, since stearic acid is known to be an effective lubricant for stainless steel. [93,94]

If the electrodeposit is rinsed with water, the sample must dry before it comes in contact with the water-insoluble stearic acid solution to prevent precipitation. However, during that drying process, Zn reacts with moisture and electrolyte salts in a way that destroys the poor water-adhesion properties of the deposit, even after coating with stearic acid to lower the surface energy. On these stearic-acid-coated water-rinsed samples, water droplets adhere easily all over the surface. Furthermore, the apparent static contact angles vary greatly, ranging from 90° to 135° , with the lowest contact angles occurring in the impurity-phase-rich portion of the deposit.

XRD data (Figure 5.3) show that the composition of the water-rinsed electrodeposits includes both Zn metal and $\text{Zn}_5(\text{OH})_8\text{Cl}_2(\text{H}_2\text{O})$, (simonkolleite, JCPDS card: 98-000-7203, with $a = 6.3412 \text{ \AA}$, $c = 23.6460 \text{ \AA}$). This composition is consistent with EDX data (not shown), which confirmed the presence of Cl and additional O in the deposit. Profilometer data (Figure 5.4) indicates that this hydroxide product alters the topography of the electrodeposit by introducing features that are $\sim 10 \mu\text{m}$ tall, and these tall features do not develop uniformly across the sample. This is consistent with inspection by eye, which shows mm-cm sized regions where the dark grey electrodeposit turns white.

The formation of this impurity phase is not surprising. Based on the thermodynamics of Zn speciation calculated by others, [67] zinc hydroxychloride precipitates

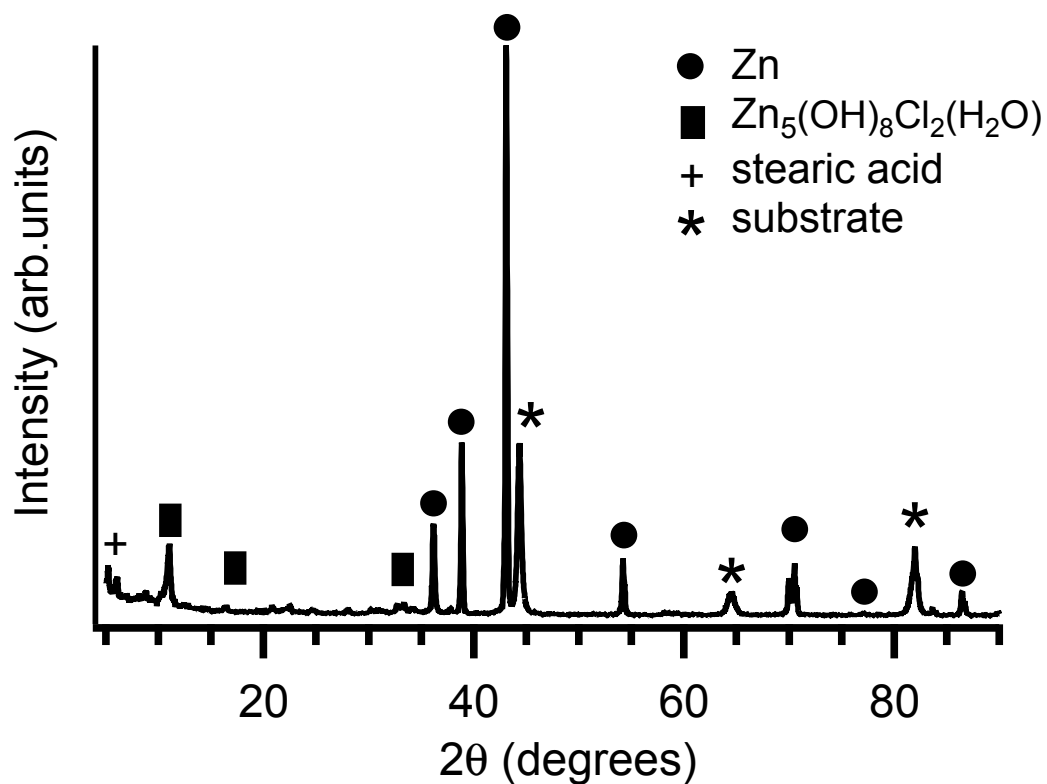


Figure 5.3: Representative XRD data for a water-rinsed electrodeposit that shows evidence of $\text{Zn}_5(\text{OH})_8\text{Cl}_2(\text{H}_2\text{O})$ (JCPDS 98-000-7203) in addition to metallic Zn (JCPDS 98-000-0482).[92] The asterisk (*) denotes peaks due to the stainless steel substrate, and plus (+) denotes a peak related to stearic acid.

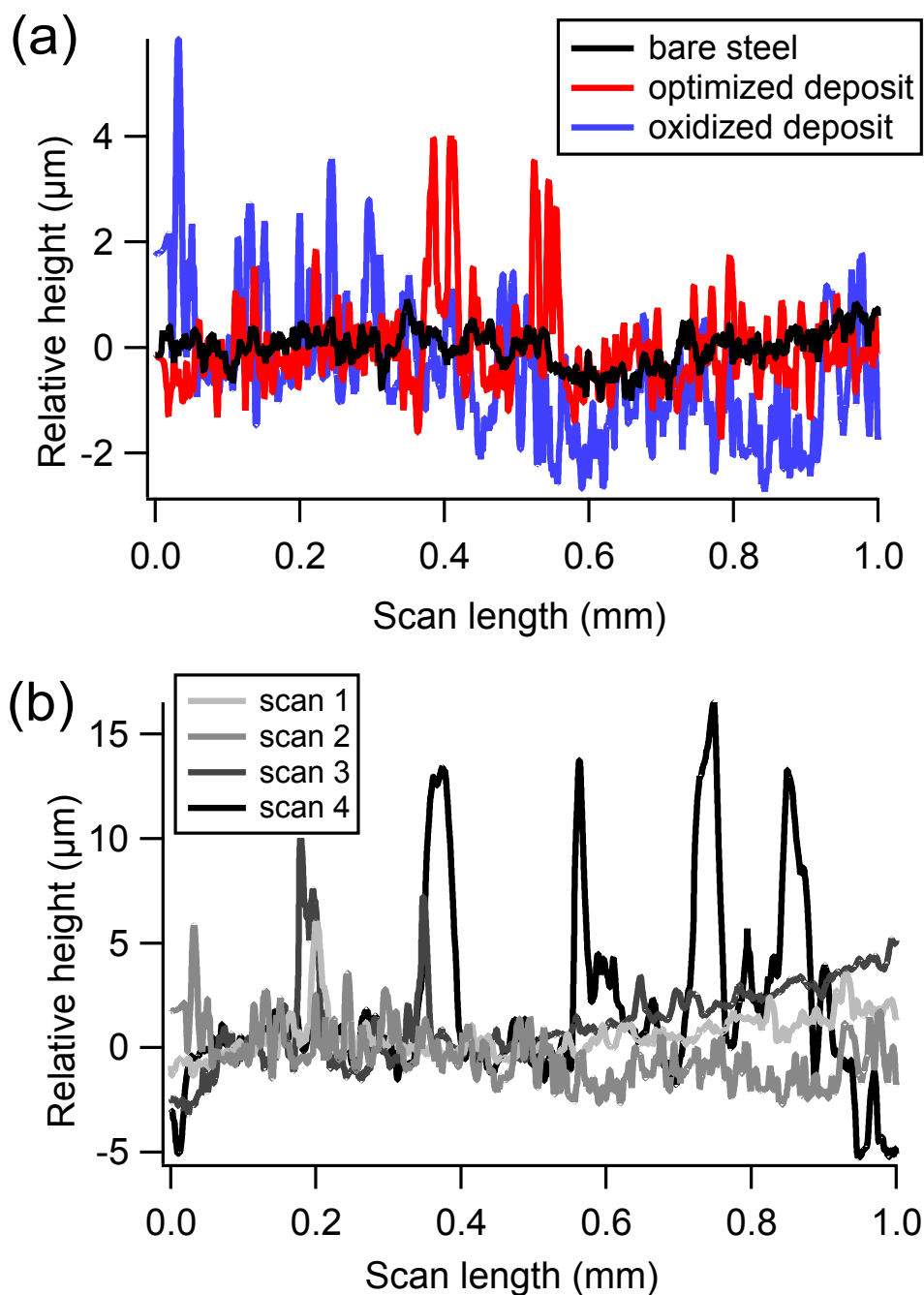


Figure 5.4: Representative profilometer scans of (a) bare stainless steel (black), ethanol-rinsed electrodeposit (red), and water-rinsed electrodeposit (blue). Corresponding root-mean-square (rms) roughness values are (in units of μm): 1.0 ± 0.3 , 2.0 ± 0.9 , and 4.0 ± 0.8 . In (b), four different scans of a single water-rinsed electrodeposit are compared. Corresponding root-mean-square (rms) roughness values are (in units of μm): 2 ± 1 , 4 ± 1 , 5 ± 2 , and 8 ± 4 .

appear near neutral pH for low concentrations of Cl^- or NH_3 (≤ 1 M) or for very high Zn concentrations (≥ 1.93 M). By going to more alkaline conditions, $\text{Zn}(\text{NH}_3)_4^{2+}$ becomes the dominant species in the electrolyte, which increases Zn^{2+} solubility and reduces hydroxide precipitation. This is consistent with the precipitate formation and disappearance that we observed when our electrolyte pH was adjusted from slightly acidic levels to a slightly alkaline range. However, we note that this precipitation behaviour occurred even though we used a low Zn concentration (0.2 M Zn^{2+}) and high Cl^- and NH_3 concentrations (≥ 3.5 M).

5.3.4 Interactions with water droplets

Upon visual inspection of the optimized stearic-acid-coated electrodeposits, it was immediately obvious that there was virtually no adhesion of macroscopic water droplets over large (cm-scale) areas. Water that squirted from a squeeze bottle or a syringe onto the surface bounced off and did not stick, except on the very edges of the substrate. Images from a more controlled version of this experiment are shown in Figure 5.5. In the top row, a needle was used to bring a 5 μL water droplet down to touch the electrodeposit surface. When the needle lifted, the water droplet remained on the needle instead of sticking to the electrodeposit. A similar response occurs when a droplet was dragged across the surface, as shown in the middle row of Figure 5.5. Along most parts of the surface, the droplet remained affixed to the needle while being dragged across cm-scale distances. However, there were a few places on each 9 cm^2 surface where the droplet was pulled off the needle and adhered to the surface; an example of this is shown in the bottom row of Figure 5.5. It is only at these anomalous "sticky" spots where the static contact angle could be measured, with typical values of $140 \pm 5^\circ$. (For comparison, the apparent static contact angle of water on the bare stainless steel is $74 \pm 3^\circ$.) Over the vast majority of the electrodeposit area, poor

droplet adhesion prevented measurement of a static contact angle because the droplet rolled off the sample.

Although it is hard to design surfaces with poor water droplet adhesion *a priori*, empirical evidence in the literature shows that such surfaces have a synergy of micrometer-scale roughness and low surface energy. [78, 79, 81] In the case of our electrodeposits, SEM images indicate that the surface topography was dramatically changed after electrodeposition. However, the resulting surface topographies are very intricate and are not easily quantified accurately across all relevant length-scales (nanometer to micrometer) with scanning probe methods. Profilometer data (Figure 5.4a) indicates that, over a 1 mm length scale, the root-mean-square (rms) roughness of the electrodeposit is $2.0 \pm 0.9 \mu\text{m}$, which is higher than the roughness of the bare stainless steel ($1.0 \pm 0.3 \mu\text{m}$). Based on this correlation between higher rms roughness and better water repellency, it is tempting to conclude that an rms roughness value difference is sufficient to explain the variations in water repellency between our optimized and less-perfect samples. However, this simple correlation is misleading because our coatings have roughnesses that vary across different length scales. To illustrate this point more clearly, Figure 5.4b shows four scans on different regions of an oxidized electrodeposit. The rms roughness values of these four scans are (in units of μm): 2 ± 1 , 4 ± 1 , 5 ± 2 , 8 ± 4 . This shows that oxidized samples have roughness heterogeneity at length scales longer than 1 mm that are not captured clearly in a single rms roughness value. Recent work by others [95] has shown that fractal models of roughness across many length scales can, in principle, be correlated with surface wettability. It would be an interesting future study, going beyond the scope of the present work, to explore whether roughness across many length scales could also be correlated with liquid droplet adhesion and water repellency as well.

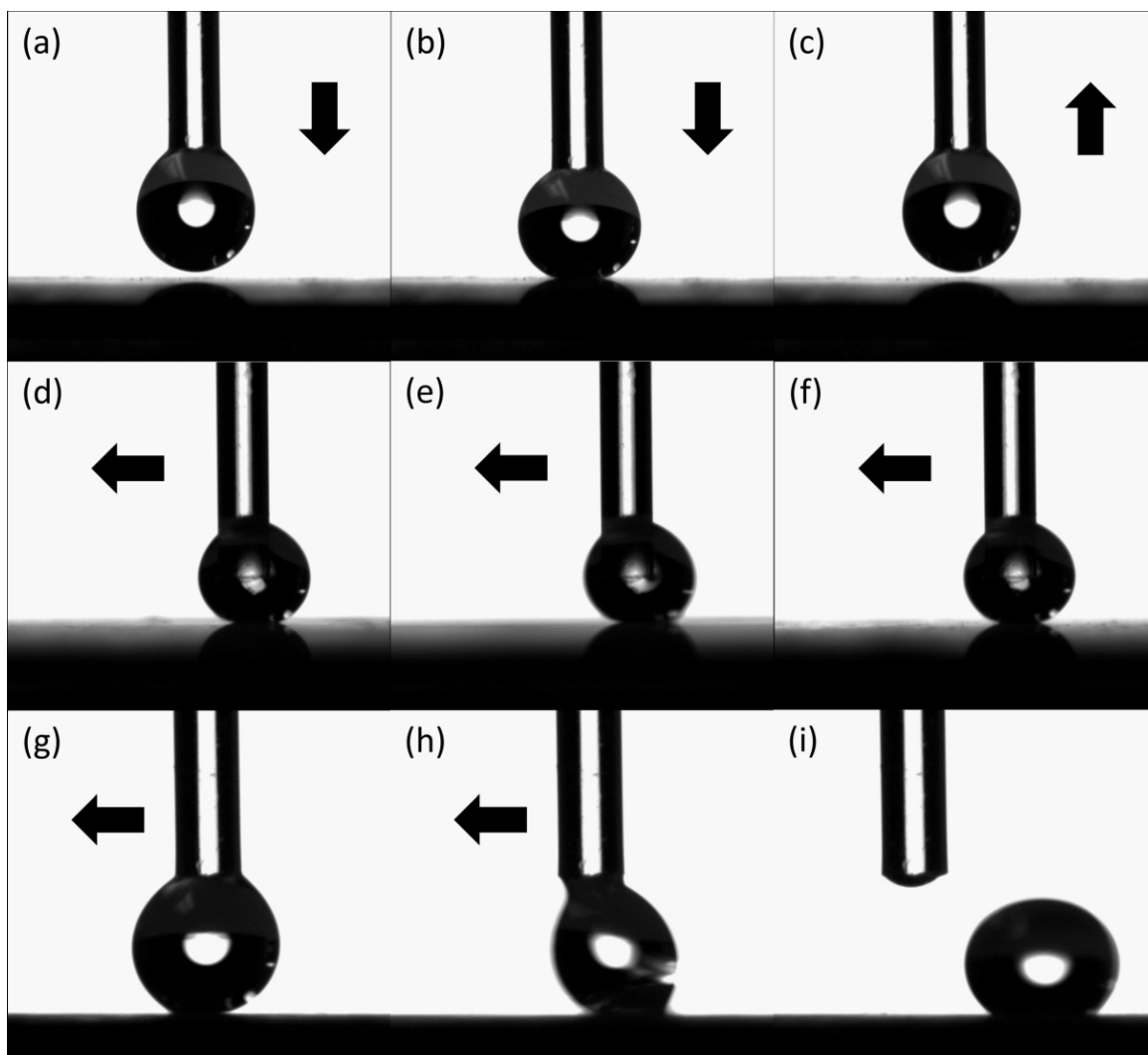


Figure 5.5: Representative image sequences of water droplets being moved across electrodeposit surfaces. For (a-c), a water droplet at the end of a syringe is brought into contact and then lifted from the electrodeposit. For (d-f), a similar droplet was slid across the surface without sticking. For (g-i), a sliding droplet was pinned to an inhomogeneity on the electrodeposit and was detached from the syringe needle.

5.3.5 Discussion of water adhesion on electrodeposits

It is worthy to note that not all hydrophobic surfaces show poor water droplet adhesion. In general, hydrophobic surfaces are defined to be those on which water droplets have static contact angles greater than 90° . However, there is often quite a range of contact angles that are measured because droplets can be pinned by chemical or topological heterogeneities on the surface. A more complete description of surface wettability involves measuring the contact angles of dynamic droplets, by adding water volume to the droplet until the water/solid contact line advances (to assess the maximum advancing contact angle) and then removing water volume from the droplet until the water/solid contact line recedes (to assess the minimum receding contact angle). [82] Others have used these advancing and receding angles to describe water repellency in terms of the force required to start a drop sliding on a surface (shear hydrophobicity) or the force required to remove a hanging drop from a surface (tensile hydrophobicity). [81]

In the case of our electrodeposits, macroscopic water droplets ($5 \mu\text{L}$ with 2 mm diameter) never adhered to most parts of the surface, making it impossible to do standard static and dynamic contact angle measurements. This suggests that, in those regions of the electrodeposit, the force needed to remove a droplet from the surface, in either tensile mode (hanging droplet, Figure 5.5a-c)s or shear mode (droplet sliding, Figure 5.5c-f) is exceedingly low.

Even though there exist models to quantify droplet adhesion on surfaces, there are no definitive strategies for predicting (or explaining) which combinations of surface features will produce a water-repellent surface. [82] In this way, any recipes for producing water-repellent surfaces offer opportunities to augment our phenomenological understanding. There are some reports of water-repellent electrodeposits, which tend to involve micrometer-scale roughened surface topographies capped with organic

coatings. For example, Cu-based electrodeposits with complex multi-scale surface features, when coated with stearic acid, repel 10 μL water droplets. [95] Zn-Ni electrodeposits, etched with NaOH to change the surface roughness and then coated with myristic acid, repel water droplets that have volumes of 10s of μL . [29] Water droplets with μL volumes also slide easily off anodically produced CuO needles with fluoroalkyl-silane surface modification. [26] This suggests that many different kinds of surface topographies and chemistries can be effective for water-repellency, and that electrodeposition can play a useful role.

5.4 Conclusions

We show that Zn electrodeposits can improve the water repellent properties of stainless steel by reducing water droplet adhesion in a dramatic fashion. There is a relatively narrow range of electrolyte pH and deposition potentials that will yield optimized deposits. This is consistent with Pourbaix diagrams, calculated by others, that are based on speciation and solubility trends for different Zn(II) complexes that form in the presence of chloride and ammonia. Capping the Zn electrodeposits with stearic acid is essential to prevent oxidation and to provide a lower surface energy for water repellency.

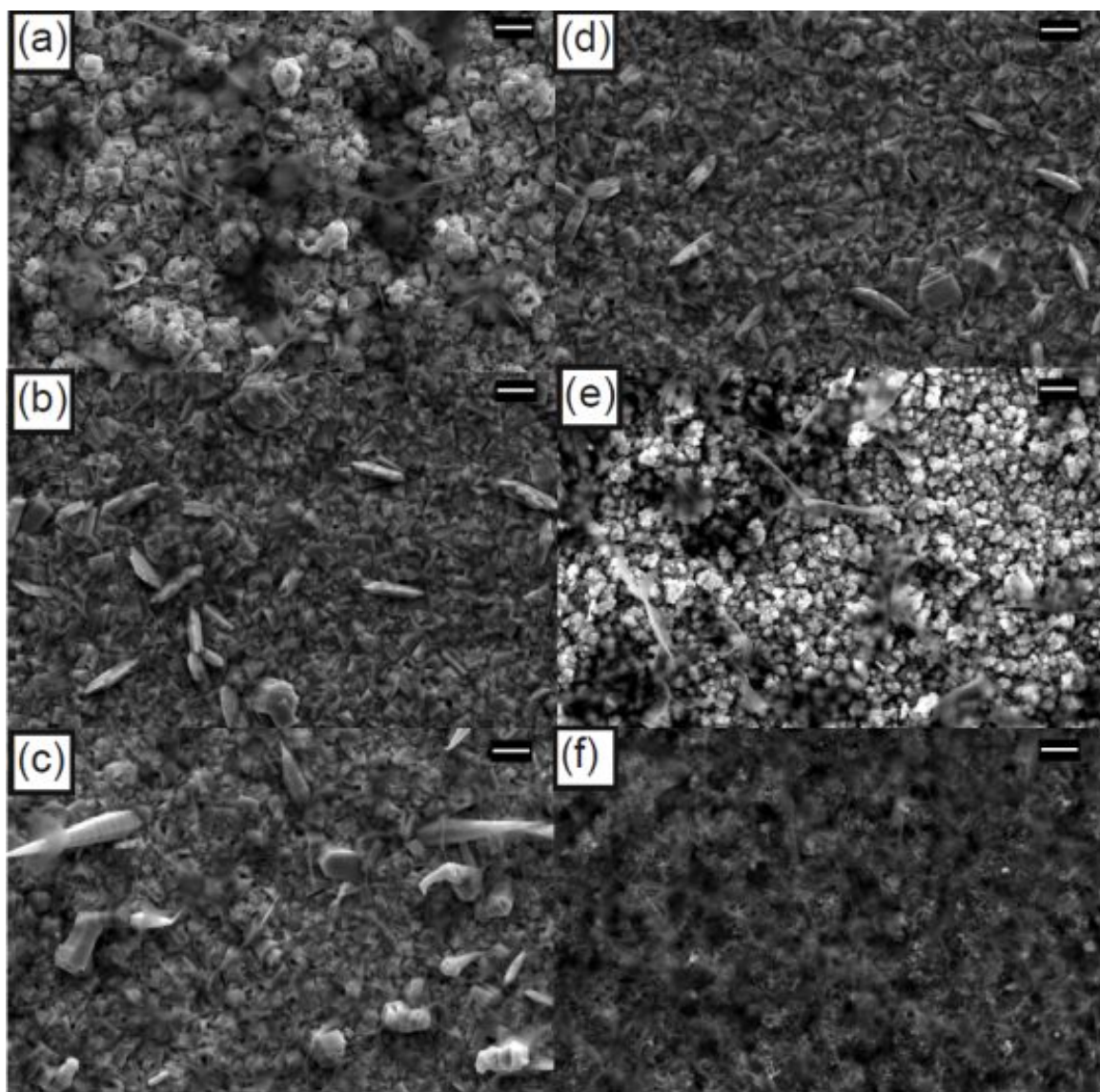


Figure 5.6: Representative SEM images of Zn electrodeposits. At constant deposition potential (-1.5 V), more alkaline pH values ((a) at 7.5) affect size and shape relative to more neutral pH ((b) at 8.0 and (c) at 8.5). Keeping the same pH value (8.0) and making the deposition potential less negative leads to more uniform crystallite sizes and shapes ((d) at -1.5 V, (e) at -1.4 V, (f) at -1.3 V). Scale bars for all SEM images are 2 μm .

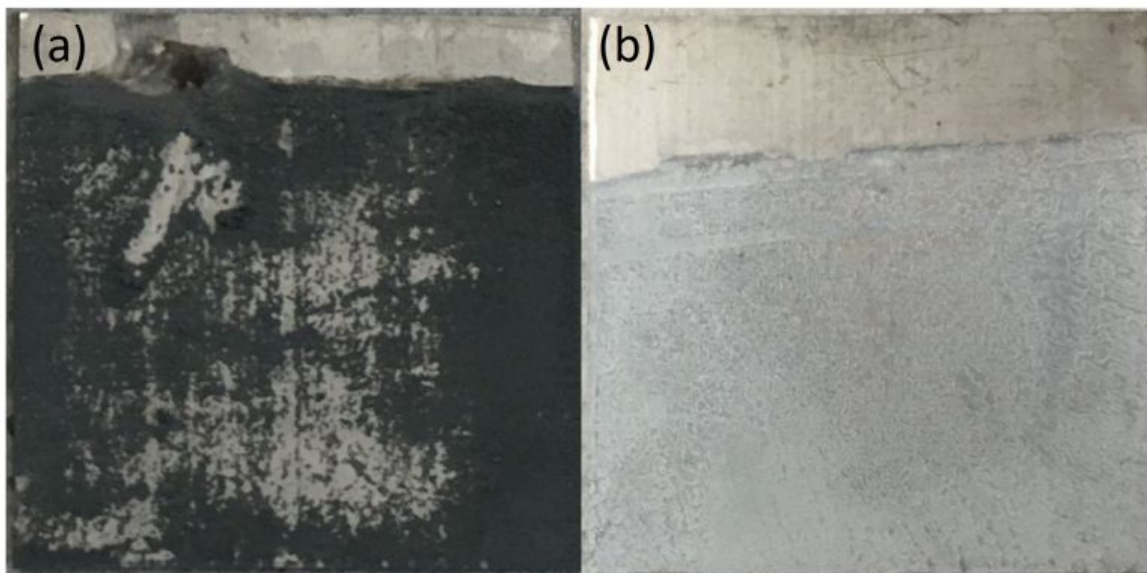


Figure 5.7: Photographs of a: zinc electrodeposit on stainless steel (-1.3 V), and b: zinc electrodeposit on stainless steel (-1.5 V). Dimensions of the plates: 3 cm x 3 cm.

5.5 Supporting information

This section is related to Chapter 5, but was not submitted to the journal.

5.5.1 Deposits on larger substrates

A low adhesion surface can be fabricated on a small stainless steel bar, but we also applied this to a larger area stainless steel surface. Stainless steel (SAE 630/ 17-4, 1 mm thickness) that is rich in Cr, Ni, and Cu was cut into 3 cm \times 3 cm squares, and we tried the same electrodeposition procedure. Due to the larger area of the working electrode, Zn failed to cover the whole surface of the substrate even when the applied potential was more negative (-1.5 V). In Figure 5.7a, a zinc electrodeposit formed at -1.3 V after 1 hour. A loose zinc film partially covered the substrate and easily rinsed off. At -1.5 V (Figure 5.7b), a 10 min deposition still did not totally cover the substrate. However, the Zn adhered better.

5.5.2 Optical images of electrodeposits

From the optical image in Figure 5.8a, the optimized coating is uniform in terms of color. For the oxidized zinc coating (Figure 5.8b), the color varies, especially at the edge of the substrate where the color is darker. The static contact angle of water droplets on the dark parts is much smaller than for droplets placed on white parts.

5.5.3 Electron-based characterization

Back-scattered electron (BSE) and energy-dispersive X-ray (EDX) analyses helped to support the XRD results.

In Figure 5.9a, a BSE image shows us that almost all parts of the film have the same brightness, which means there is similar elemental content across the film. From the EDX plot, it is not surprising to see the existence of Zn. The appearance of C and O likely comes from the stearic acid coating. Therefore, both BSE and EDX indicate that the optimized zinc coating is composed of zinc crystallites and stearic acid.

In Figure 5.9b, there are totally different colors across the BSED image. The white part indicates heavier elements. The black part indicates lighter elements. For the white part, the EDX plot shows the high intensity of Zn and C. For the black part, the intensity of O increases considerably. The more important finding is the existence of Cl, which suggests that the oxidized zinc coating contains $\text{Zn}_5(\text{OH})_8\text{Cl}_2(\text{H}_2\text{O})$, as shown in the XRD data (Figure 5.3).

5.5.4 Self-cleaning behaviour

Since our zinc coatings have poor water adhesion, self-cleaning behaviour is obtainable. As shown in Figure 5.10, some salts were placed on the zinc coating, then water droplets were dropped on the surface. Water droplets easily roll off and remove salts

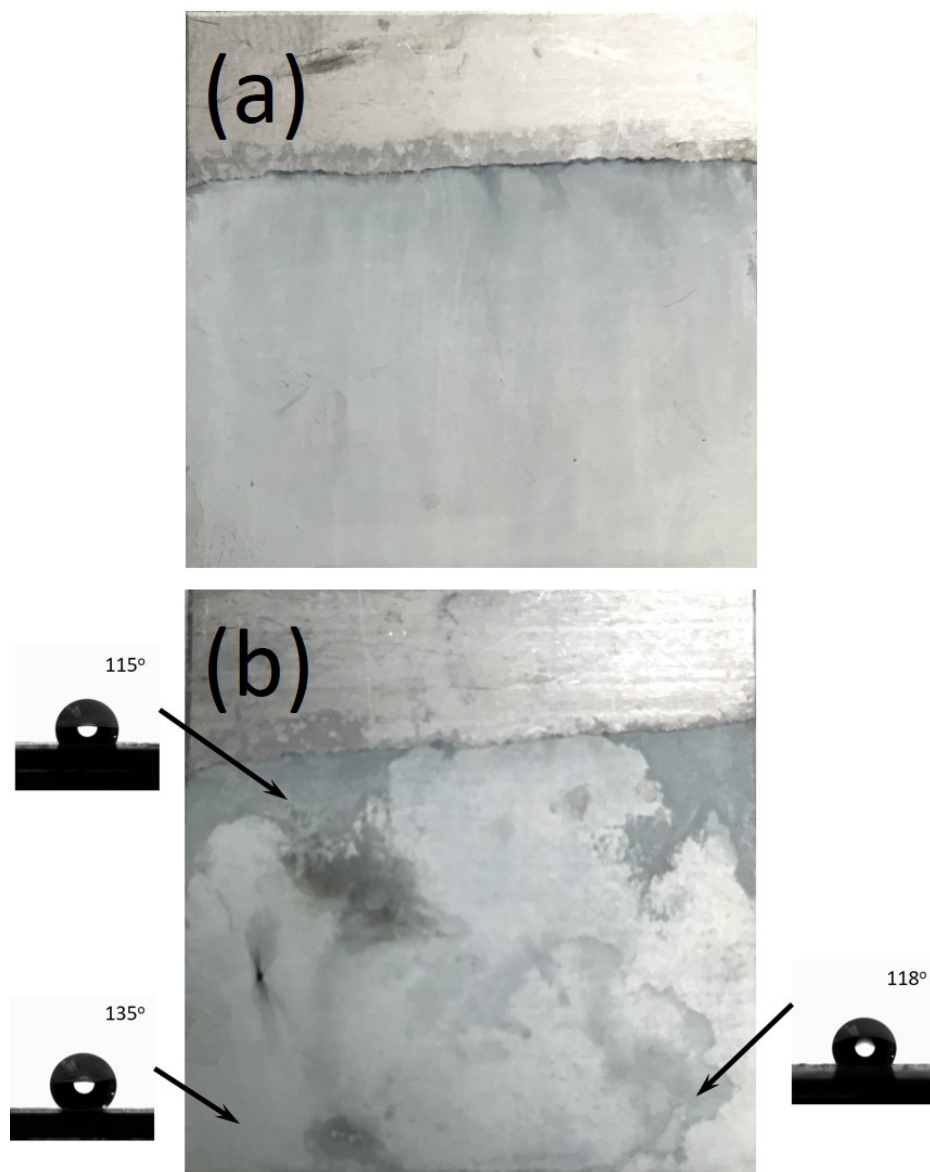


Figure 5.8: Optical images of a: optimized zinc coating, and b: oxidized zinc coating. Dimensions of the plates: 3 cm x 3 cm.

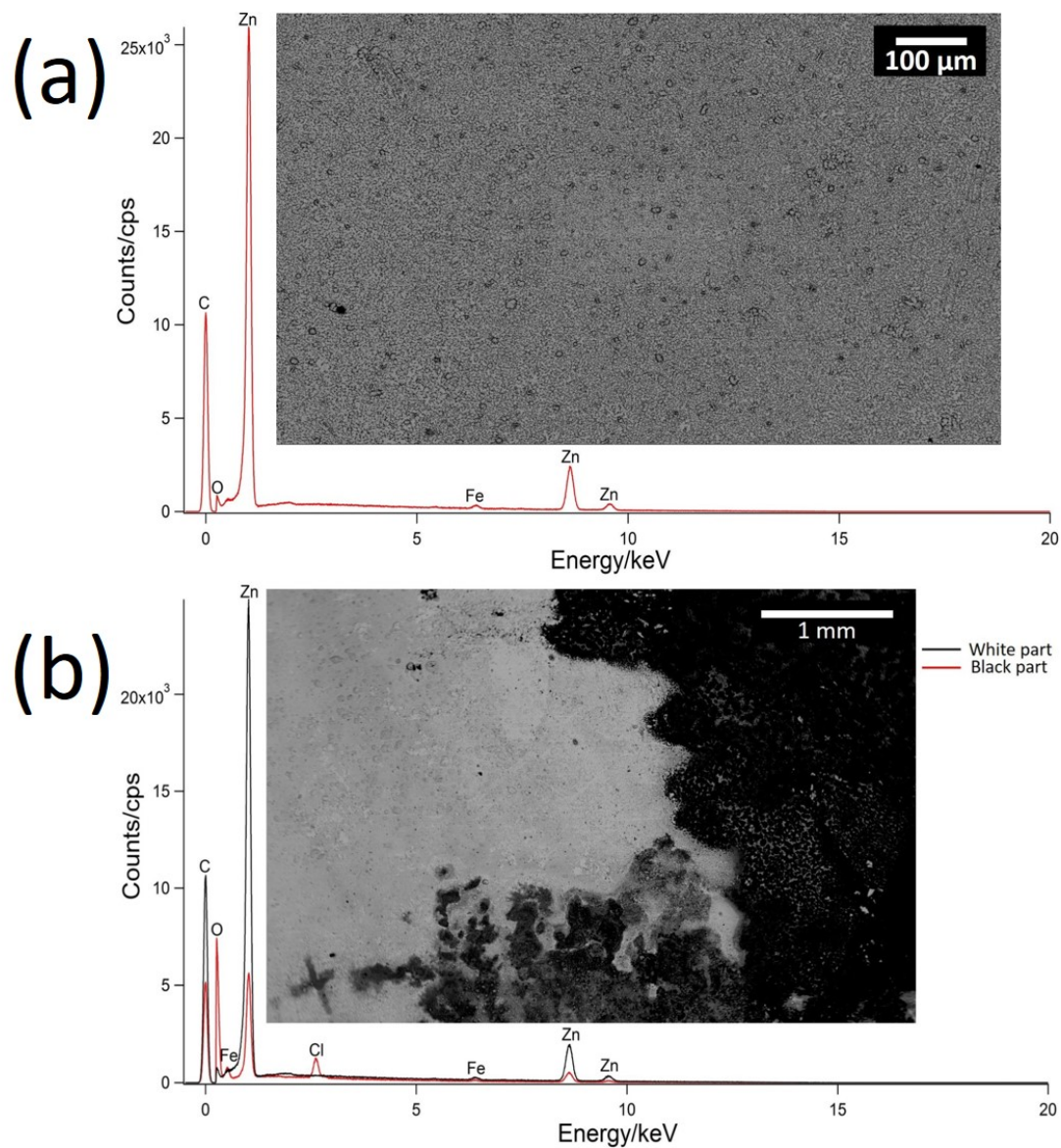


Figure 5.9: Representative back scattered electron images and energy-dispersive X-ray data for a: optimized zinc coating, and b: oxidized zinc coating.

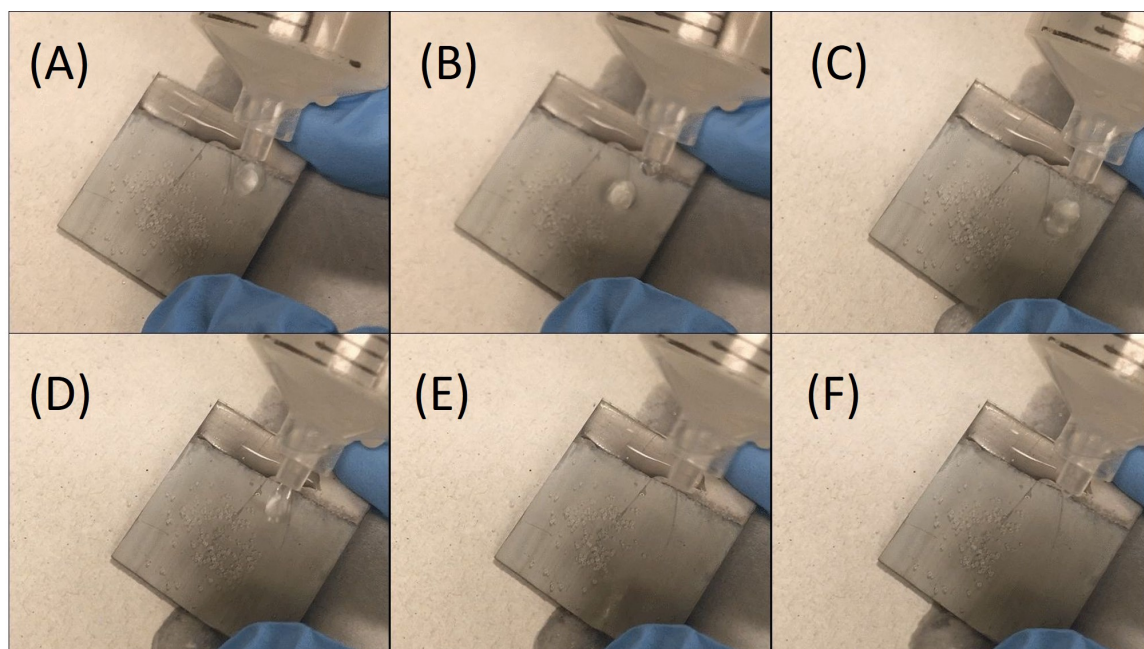


Figure 5.10: Consecutive images: the self-cleaning behaviour of our zinc coating.

from the surface, without any wetting. Thus, this material is an effective self-cleaning surface.

Chapter 6

Conclusions and future work

6.1 Conclusions

In recent years, water-repellent surfaces have attracted much attention for use in various applications. Based on the Cassie-Baxter model, we know that surface roughness, and low surface energy, need to be present to generate a hydrophobic surface. However, the Cassie-Baxter model is a simple model, that can only be applied to a regular rough surface. Moreover, the Cassie-Baxter model doesn't say anything about the adhesion between the liquid and solid interface. Even for a surface that is considered superhydrophobic, strong adhesion can make water droplets stick easily on the surface. For offshore engineering metals, reducing droplet adhesion is very desirable. It is still an open research question to answer what structural characteristics have optimized low adhesion properties. As a chemist, I tried to use a chemical method to change the way water interacts with steel, so as to fabricate a low adhesion material.

In my research project, increasing surface roughness and reducing surface energy are two goals I needed to achieve. For surface energy changes, organic coatings were investigated. Three organic coatings (stearic acid, dodecanethiol, Aculon) were coated

on engineering steels. The second goal was increasing the surface roughness. Chemical etching and zinc electrodeposition were used to achieve this goal. A steel surface has a high surface energy. From the Wenzel model, we know that if the original surface is a hydrophilic surface, then the corresponding rough surface would become more hydrophilic. Therefore, surface roughness had to be combined with organic coatings to make the surface repel water better.

The main conclusions of this thesis are summarized as follows:

- Organic coated surfaces are more hydrophobic than the original steel surface, which is not surprising. However, the contact angle varies a lot at different positions on a surface, which reflects heterogeneous adhesion of the organic coating to the steel. Organic coated surfaces still have strong droplet adhesion, just like the uncoated steel.
- With chemical etching, the static contact angles of organic coated surfaces become larger. Moreover, the spread of static contact angle values becomes smaller, which means chemical etching not only change the surface roughness, but also makes the organic coating more uniform on the surface. However, the phenomenon of strong droplet adhesion still occurs even with the combination of chemical etching and organic coating.
- Zn electrodeposits with stearic acid coating surface have topography and chemistry that give rise to remarkable low adhesion behaviour.
 - Zn electrodeposit on steel increases the surface roughness.
 - The addition of PEI surfactant can alter the evolution of hydrogen gas during electrodeposition, so as to allow complete Zn coverage on the surface.
 - pH and potential are two important factors that change the electrodeposit topography, which influences the water adhesion behaviour.

- Stearic acid not only lowers the surface energy, but also protects Zn deposits from contamination by the ambient atmosphere.
- The good low adhesion behaviour lends itself to the application of self-cleaning.

6.2 Future work

We already showed that our zinc electrodeposits are effective at water self-cleaning behaviour. We would like to investigate whether our zinc electrodeposit are also anti-icing surfaces.

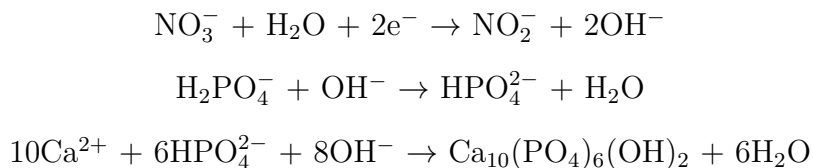
There are many other methods that can be used to increase surface roughness, such as sandblasting. In the future, we want combine mechanical methods with zinc electrodeposition for different surface roughening. Some progress has been made. We deposited our zinc coatings on sandblasted steel. The low adhesion behaviour seems improved based on preliminary results. Water droplets can roll off more easily on sandblast-zinc coated surface than on zinc-stearic acid coated surface. However, we still need to find a way to quantify differences among the adhesion behaviours of different samples.

Appendix A

Studies of other electrodeposits

A.1 Calcium phosphate

Calcium phosphate, an inorganic mineral, is of great interest due to its biocompatibility [96,97]. Moreover, electrodeposition is a promising method to fabricate calcium phosphate. During galvanostatic electrodeposition, two major phases form: brushite ($\text{CaHPO}_4 \cdot \text{H}_2\text{O}$) and hydroxyapatite ($\text{Ca}_{10}(\text{PO}_4)_6(\text{OH})_2$) [98]. Based on previous work, hydroxyapatite is dominant during electroprecipitation when the concentration of phosphate in the electrolyte is lower than 0.03 M [99]. The mechanism for hydroxyapatite precipitation is shown below.



A.1.1 Previous material

In 2006, there were previous Poduska group members, Stephanie D. Huelin and Holly R. Baker, who fabricated hydroxyapatite on a small piece of stainless steel by elec-

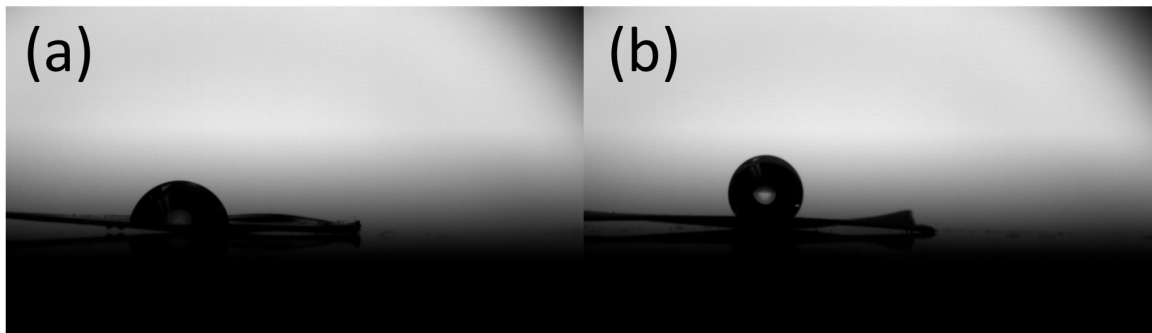


Figure A.1: Photograph of a 5 μL water droplet on (a): bare stainless steel (contact angle = $79 \pm 1^\circ$), and (b): calcium phosphate electrodeposit (contact angle = $127 \pm 1^\circ$).

trodeposition [99]. I tested the static contact angle of this sample that was produced 11 years ago. Due to the small substrate size, we have only one contact angle value for each sample. Therefore, uncertainties (error bars) are based on how well the left and right contact angles agree in a single image of a droplet. As shown in Figure A.1, the water contact angle on original stainless steel was $79 \pm 1^\circ$, whereas for the droplet on hydroxyapatite, the contact angle was $127 \pm 1^\circ$. Therefore, this material interested us for further study.

A.1.2 Experimental section

Following experimental procedures by others [99], we electrodeposited calcium phosphate on stainless steel to test its hydrophobicity.

Potassium phosphate (monobasic) (7 g in 50 ml) was dissolved in water. Then a mixture of potassium phosphate solution and 1 M calcium nitrate solution generated white precipitate. After complete precipitation, the supernatant was poured off and the precipitate was dissolved in 1 M nitric acid solution. Finally, ammonium sulfate was added to make the concentration of NH_4^+ 0.1 M. The pH of the final solution was near 2. Electrodeposition was carried out using a Hokuto Denko Model HA-501

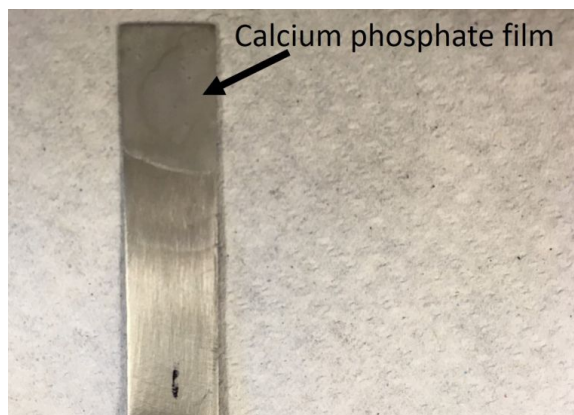


Figure A.2: Photograph of calcium phosphate electrodeposit.

potentiostat with three electrodes (steel as WE, carbon rod as RE and saturated calomel electrode as RE). A hydroxyapatite film was fabricated at the current density of 30 mA/cm^2 for a deposition time of 60 min. The initial potential was near -0.68 V . After 1 h, the potential increased to -1.52 V .

A.1.3 Preliminary results

A very uniform calcium phosphate film forms on stainless steel, shown in Figure A.2. However, we didn't get high contact angles on this surface. We need to investigate the structure of the electrodeposit and try to combine calcium phosphate with organic coatings to see if this could be another promising water-repellent coating.

Bibliography

- [1] Mingjie Liu, Shutao Wang, and Lei Jiang. Nature-inspired superwettability systems. *Nature Reviews Materials*, 2, 2017.
- [2] Girish Kumar and K. Narayan Prabhu. Review of non-reactive and reactive wetting of liquids on surfaces. *Advances in Colloid and Interface Science*, 133(2):61–89, 2007.
- [3] Luisa Peraldo Bicelli, Benedetto Bozzini, Claudio Mele, and Lucia D’Urzo. A review of nanostructural aspects of metal electrodeposition. *International Journal of Electrochemical Science*, 3(4):356–408, 2008.
- [4] A. D. Davydov and V. M. Volgin. Template electrodeposition of metals. review. *Russian Journal of Electrochemistry*, 52(9):806–831, Sep 2016.
- [5] Paula Gould. Smart, clean surfaces. *Mater. Today.*, 6(11):44–48, 2003.
- [6] Haiping Tian, Jingxian Zhang, Erdan Wang, Zhaohui Yao, and Nan Jiang. Experimental investigation on drag reduction in turbulent boundary layer over superhydrophobic surface by TRPIV. *Theor. Appl.*, 5(1):45–49, 2015.
- [7] Liangliang Cao, Andrew K. Jones, Vinod K. Sikka, Jianzhong Wu, and Di Gao. Anti-Icing superhydrophobic coatings. *Langmuir*, 25(21):12444–12448, 2009.

- [8] Kevin Golovin, Sai P.R. Kobaku, Duck Hyun Lee, Edward T. DiLoreto, Joseph M. Mabry, and Anish Tuteja. Designing durable icephobic surfaces. *Sci. Adv.*, 2(3):1–12, 2016.
- [9] Adel M.A. Mohamed, Aboubakr M. Abdullah, and Nathalie A. Younan. Corrosion behavior of superhydrophobic surfaces: A review. *Arab. J. Chem.*, 8(6):749–765, 2015.
- [10] Takahiro Ishizaki and Michiru Sakamoto. Facile formation of biomimetic color-tuned superhydrophobic magnesium alloy with corrosion resistance. *Langmuir*, 27(6):2375–2381, 2011.
- [11] Ke Peng and Wang Xinxin. Super-cooled large droplets consideration in the droplet impingement simulation for aircraft icing. *Procedia Engineering*, 17:151–159, 2011.
- [12] Christine Malmos Perfeltdt, Hassan Sharifi, Nicolas von Solms, and Peter Englezos. Oil and gas pipelines with hydrophobic surfaces better equipped to deal with gas hydrate flow assurance issues. *J. Nat. Gas. Sci. Eng.*, 27:852 – 861, 2015.
- [13] Baeyer Hans Christian. The lotus effect. *The Sciences*, 40(1):12–15, 2000.
- [14] Henry Margenau. Surface energy of liquids. *Phys. Rev.*, 38:365–371, Jul 1931.
- [15] B. J. Keene. Review of data for the surface tension of pure metals. *Int. Mater. Rev.*, 38(4):157–192, 1993.
- [16] Daniel Bonn, Jens Eggers, Joseph Indekeu, Jacques Meunier, and Etienne Rolley. Wetting and spreading. *Rev. Mod. Phys.*, 81:739–805, May 2009.
- [17] P. G. de Gennes. Wetting: statics and dynamics. *Rev. Mod. Phys.*, 57:827–863, Jul 1985.

- [18] Klaus Kern, Rudolf David, Robert L. Palmer, and George Comsa. Complete wetting on “strong” substrates: Xe/pt(111). *Phys. Rev. Lett.*, 56:2823–2826, Jun 1986.
- [19] Prashant V. Kamat. Physical chemistry at the interface. *J. Phys. Chem. Lett.*, 6(24):5093–5093, 2015.
- [20] T. Young. An Essay on the Cohesion of Fluids. *Philosophical Transactions of the Royal Society of London*, 95(0):65–87, 1805.
- [21] Robert H. Dettre and Rulon E. Johnson. Contact Angle Hysteresis. IV. Contact Angle Measurements on Heterogeneous Surfaces. *J. Phys. Chem.*, (5):1507–1515.
- [22] Robert N. Wenzel. Resistance of solid surfaces to wetting by water. *Ind. Eng. Chem.*, 28(8):988–994, 1936.
- [23] A. B. D. Cassie. Contact angle. *Discuss. Faraday Soc*, 3:11–16, 1948.
- [24] A. B. D. Cassie and S. Baxter. Wettability of porous surfaces. *Trans. Faraday Soc*, 40:546–551, 1944.
- [25] Yi Fan, Yi He, Pingya Luo, Xi Chen, and Bo Liu. A facile electrodeposition process to fabricate corrosion-resistant superhydrophobic surface on carbon steel. *Appl. Surf. Sci.*, 368:435–442, 2016.
- [26] Feng Xiao, Shaojun Yuan, Bin Liang, Guanqiu Li, Simo Olavi Pehkonen, and TieJun Zhang. Superhydrophobic CuO nanoneedle-covered copper surfaces for anticorrosion. *J. Mater. Chem. A*, 3(8):4374–4388, 2015.
- [27] N. P. Klochko, K. S. Klepikova, V. R. Kopach, G. S. Khrypunov, Yu. O. Myagchenko, E. E. Melnychuk, V. M. Lyubov, and A. V. Kopach. On Control-

- ling the Hydrophobicity of Nanostructured Zinc-Oxide Layers Grown by Pulsed Electrodeposition. *Semiconductors*, 50(3):352–363, 2016.
- [28] Mei Li, Jin Zhai, Huan Liu, Yanlin Song, Lei Jiang, and Daoben Zhu. Electrochemical Deposition of Conductive Superhydrophobic Zinc Oxide Thin Films. *J.Phys. Chem. B*, 107(37):9954–9957, 2003.
- [29] Tengfei Xiang, Manxin Zhang, Cheng Li, Shunli Zheng, Shibing Ding, Jing Wang, Chundong Dong, and Ling Yang. A facile method for fabrication of superhydrophobic surface with controllable water adhesion and its applications. *J. Alloy. Compd.*, 704:170–179, 2017.
- [30] Dandan Lv, Hongfei Shao, Xiang Gao, Ke Lu, Haifeng Lu, and Houyi Ma. Fabrication and corrosion resistance properties of super-hydrophobic coatings on iron and steel substrates by creating micro-/nano-structures and modifying rough surfaces. *RSC Advances*, 6(96):93419–93427, 2016.
- [31] Milton Stern. Electrochemical Polarization. *J. Electrochem. Soc.*, 104(9):559, 1957.
- [32] R. H. Brown and R. B. Mears. The Electrochemistry of Corrosion. *T. Electrochem. Soc.*, 74(1):495, 1938.
- [33] E. McCafferty. Validation of corrosion rates measured by the Tafel extrapolation method. *Corros. Sci.*, 47(12):3202 – 3215, 2005. A Century of Tafel’s Equation: A Commemorative Issue of Corrosion Science.
- [34] G.T. Burstein. A hundred years of Tafel’s equation: 1905–2005. *Corros. Sci.*, 47(12):2858 – 2870, 2005. A Century of Tafel’s Equation: A Commemorative Issue of Corrosion Science.

- [35] R.F. Mann, J Amphlett, Brant Peppley, and Chris Thurgood. Application of Butler–Volmer equations in the modelling of activation polarization for PEM fuel cells. *J. Power. Sources.*, 161:775–781, 10 2006.
- [36] Tz. Tzvetkoff, A. Girginov, and M. Bojinov. Corrosion of nickel, iron, cobalt and their alloys in molten salt electrolytes. *J. Mater. Sci.*, 30(22):5561–5575, Jan 1995.
- [37] Harvey J. Flitt and D. Paul Schweinsberg. A guide to polarisation curve interpretation: Deconstruction of experimental curves typical of the Fe/H₂O/H⁺/O₂ corrosion system. *Corros. Sci.*, 47(9):2125–2156, 2005.
- [38] J. G. Brown. Diffraction of X-rays. *X-Rays and Their Applications*, pages 95–121, 1966.
- [39] W. L. Bragg W. H. Bragg. The reflection of X-rays by crystals. *P. Roy. Soc. Lond. A. Mat.*, 88(605):428–438, 1913.
- [40] J Goldstein, Dale E. Newbury, Joseph Michael, Nicholas Ritchie, John Henry J. Scott, and David C. Joy. *Scanning Electron Microscopy and X-Ray Microanalysis*. Springer US, 01 2018.
- [41] D. A. Moncrieff and P. R. Barker. Secondary electron emission in the scanning electron microscope. *Scanning*, 1(3):195–197, 1978.
- [42] A. O. Barut. The mechanism of secondary electron emission. *Phys. Rev.*, 93:981–984, Mar 1954.
- [43] Yasuyuki Okano. *Scanning Electron Microscopy*, pages 563–569. Springer Singapore, Singapore, 2018.

- [44] Milan Milosevic. On the nature of the evanescent wave. *Appl. Spectrosc.*, 67(2):126–131, 2013.
- [45] Milan Milosevic. Internal reflection and ATR spectroscopy. *Appl. Spectrosc. Rev.*, 39(3):365–384, 2004.
- [46] Beeley Wood Lane and S Sheffield. *ASTM A350 LF2 – Carbon Steel*. <http://www.abbeyforgedproducts.co.uk/images/downloads/PDF/ASTM-A350-LF2.pdf>.
- [47] Libang Feng, Hongxia Zhang, Pengzhi Mao, Yanping Wang, and Yang Ge. Superhydrophobic alumina surface based on stearic acid modification. *Appl. Surf. Sci.*, 257(9):3959–3963, 2011.
- [48] Quan Zhang, Yong Wan, Yang Li, Shuyan Yang, and Wenqing Yao. Friction reducing behavior of stearic acid film on a textured aluminum substrate. *Appl. Surf. Sci.*, 280:545–549, 2013.
- [49] Guillaume Sauthier, Juan José Segura, Jordi Fraxedas, and Albert Verdaguer. Hydrophobic coating of mica by stearic acid vapor deposition. *Colloid. Surface. A.*, 443:331–337, 2014.
- [50] Abraham Ulman. Formation and structure of self-assembled monolayers. *Chem. Rev.*, 96(4):1533–1554, 1996.
- [51] Jie Ling Lou, Hung Wei Shiu, Lo Yueh Chang, Chia Ping Wu, Yun Liang Soo, and Chia Hao Chen. Preparation and characterization of an ordered 1-dodecanethiol monolayer on bare Si(111) surface. *Langmuir*, 27(7):3436–3441, 2011.
- [52] A. Ptak, H. Gojzewski, M. Kappl, and H. J. Butt. Influence of humidity on the nanoadhesion between a hydrophobic and a hydrophilic surface. *Chem. Phys. Lett.*, 503(1-3):66–70, 2011.

- [53] Abdulla Hel Al Mamun, Sangwoon Yoon, and Jae Ryang Hahn. Influence of the molecular-scale structures of 1-dodecanethiol and 4-methylbenzenethiol self-assembled monolayers on gold nanoparticles adsorption pattern. *J. Colloid. Interf. Sci.*, 425(2):83–90, 2014.
- [54] Qinmin Pan, Min Wang, and Hongbo Wang. Separating small amount of water and hydrophobic solvents by novel superhydrophobic copper meshes. *Appl. Surf. Sci.*, 254(18):6002–6006, 2008.
- [55] Brad Graves. Aculon’s coatings make sure surface problems are covered. *San Diego Business Journal*, 37(23):4, Jun 2016. Copyright - Copyright San Diego Business Journal Jun 6-Jun 12, 2016; Last updated - 2016-06-13.
- [56] Norsok Standard. *Material data sheets for piping*, 1997. <http://www.standard.no/pagefiles/1156/m-cr-630r1.pdf>.
- [57] P. Nageswara Rao and Deepak Kunzru. Fabrication of microchannels on stainless steel by wet chemical etching. *J. Micromech. Microeng.*, 17(12), 2007.
- [58] Hongmei Zhang, Jin Yang, Beibei Chen, Can Liu, Mingsuo Zhang, and Changsheng Li. Fabrication of superhydrophobic textured steel surface for anti-corrosion and tribological properties. *Appl. Surf. Sci.*, 359:905–910, 2015.
- [59] Sanjay S. Latthe, P. Sudhagar, Anitha Devadoss, A. Madhan Kumar, Shanhu Liu, Chiaki Terashima, Kazuya Nakata, and Akira Fujishima. A mechanically bendable superhydrophobic steel surface with self-cleaning and corrosion-resistant properties. *J. Mater. Chem. A*, 3(27):14263–14271, 2015.
- [60] Sirong Yu, Xiaolong Wang, Wei Wang, Qiang Yao, Jun Xu, and Wei Xiong. A new method for preparing bionic multi scale superhydrophobic functional surface on X70 pipeline steel. *Appl. Surf. Sci.*, 271:149–155, 2013.

- [61] Lester Li, Victor Breedveld, and Dennis W. Hess. Creation of superhydrophobic stainless steel surfaces by acid treatments and hydrophobic film deposition. *ACS. Appl. Mater. Inter.*, 4(9):4549–4556, 2012.
- [62] G Zheng, B N Popov, and R E White. Use of Underpotential Deposition of Zinc to Mitigate Hydrogen Absorption into Monel K500. *J. Electrochem. Soc.*, 141(5):1220–1224, 1994.
- [63] A. Y. Hosny, M. E. El-Rafei, T. A. Ramadan, B. A. El-Gafari, and S. M. Morsy. Corrosion resistance of zinc coatings produced from a sulfate bath. *Met. Finish.*, 93(11):55–59, 1995.
- [64] Xiangtai Zhang, Jun Liang, Baixing Liu, and Zhenjun Peng. Preparation of superhydrophobic zinc coating for corrosion protection. *Colloid. Surface. A.*, 454(1):113–118, 2014.
- [65] Yi Han Chen, Hsin Wen Yeh, Nai Chang Lo, Chen Wei Chiu, I. Wen Sun, and Po Yu Chen. Electrodeposition of compact zinc from the hydrophobic Brønsted acidic ionic liquid-based electrolytes and the study of zinc stability along with the acidity manipulation. *Electrochim. Acta.*, 227:185–193, 2017.
- [66] L. E. Morón, Alia Méndez, F. Castañeda, J. G. Flores, L. Ortiz-Frade, Y. Meas, and G. Trejo. Electrodeposition and corrosion behavior of Zn coatings formed using as brighteners arene additives of different structure. *Surf. Coat. Tech.*, 205(21-22):4985–4992, 2011.
- [67] Jorge Vazquez-Arenas, Fabiola Sosa-Rodriguez, Isabel Lazaro, and Roel Cruz. Thermodynamic and electrochemistry analysis of the zinc electrodeposition in $\text{NH}_4\text{Cl-NH}_3$ electrolytes on Ti, Glassy Carbon and 316L Stainless Steel. *Electrochim. Acta*, 79:109–116, 2012.

- [68] Marcos F. De Carvalho and Ivani A. Carlos. Zinc electrodeposition from alkaline solution containing trisodium nitrilotriacetic added. *Electrochimica Acta*, 113:229–239, 2013.
- [69] Jan Dundálek, Ivo Šnajdr, Ondřej Libánský, Jiří Vrána, Jaromír Pociedič, Petr Mazúr, and Juraj Kosek. Zinc electrodeposition from flowing alkaline zincate solutions: Role of hydrogen evolution reaction. *Journal of Power Sources*, 372(August):221–226, 2017.
- [70] R. Y. Wang, D. W. Kirk, and G. X. Zhang. Effects of Deposition Conditions on the Morphology of Zinc Deposits from Alkaline Zincate Solutions. *Journal of The Electrochemical Society*, 153(5):C357, 2006.
- [71] François Berger, Joseph Delhalle, and Zineb Mekhalif. Undec-10-ene-1-thiol multifunctional molecular layer as a junction between metallic zinc and polymer coatings on steel. *Electrochimica Acta*, 54(26):6464–6471, 2009.
- [72] Paula Yurkanis Bruice. Spectroscopy tables. *Organic Chemistry*, 2620:A–16, A17, 2011.
- [73] Nadia Febiana Djaja, Dionisius Agung Montja, and Rosari Saleh. The Effect of Co Incorporation into ZnO Nanoparticles. *Advances in Materials Physics and Chemistry*, 03(01):33–41, 2013.
- [74] Maria Öhman and Dan Persson. An integrated in situ ATR-FTIR and EIS set-up to study buried metal-polymer interfaces exposed to an electrolyte solution. *Electrochim. Acta.*, 52(16):5159–5171, 2007.
- [75] Maria Öhman, Dan Persson, and Christofer Leygraf. A Spectroelectrochemical Study of Metal/Polymer Interfaces by Simultaneous In Situ ATR-FTIR and EIS. *Electrochem. Solid. St.*, 10(4):C27, 2007.

- [76] Boyang Gao and Kristin M. Poduska. Electrodeposited Zn for Water-Repellent Coatings. *Journal of The Electrochemical Society*, 165(10):D472–D476, 2018.
- [77] Adam J. Meuler, Gareth H. McKinley, and Robert E. Cohen. Exploiting Topographical Texture To Impart Icephobicity. *ACS Nano*, 12(4):7048–7052, 2010.
- [78] Michael J. Kreder, Jack Alvarenga, Philseok Kim, and Joanna Aizenberg. Design of anti-icing surfaces: smooth, textured or slippery? *Nature Rev.*, 1(1):1–15, 2016.
- [79] Reiner Füstner, Wilhelm Barthlott, Christoph Neinhuis, and Peter Walzel. Wetting and self-cleaning properties of artificial superhydrophobic surfaces. *Langmuir*, 21(3):956–961, 2005.
- [80] Abraham Marmur. From Hydrophilic to Superhydrophobic: Theoretical Conditions for Making High-Contact-Angle Surfaces from Low-Contact-Angle Materials. *Langmuir*, 24:7573–7579, 2008.
- [81] Lichao Gao and Thomas J. McCarthy. Wetting 101° . *Langmuir*, 25:14105–14115, 2009.
- [82] Yevgeniy V. Kalinin, Viatcheslav Berejnov, and Robert E. Thorne. Contact Line Pinning by Microfabricated Patterns: Effects of Microscale Topography. *Langmuir*, 25:5391–5397, 2009.
- [83] Edward Bormashenko. Progress in understanding wetting transitions on rough surfaces. *Adv. Colloid Interface Sci.*, 222:92–103, 2015.
- [84] Wu-Zhi Yuan and Li-Zhi Zhang. Lattice Boltzmann Simulation of Droplets Impacting on Superhydrophobic Surfaces with Randomly Distributed Rough Structures. *Langmuir*, 33:820–829, 2017.

- [85] Dominic J. Varacalle, Jr., Donna Post Guillen, Douglas M. Deason, William Rhodaberger, and Elliott Sampson. Effect of Grit-Blasting on Substrate Roughness and Coating Adhesion. *J. Thermal Spray Technol.*, 15:348–355, 2006.
- [86] F.J. Montes Ruiz-Cabello, A. Amirfazli, M. Cabrerizo-Vílchez, and M.A. Rodríguez-Valverde. Fabrication of water-repellent surfaces on galvanized steel. *RSC Advances*, 6(76):71970–71976, 2016.
- [87] Samuel Beckford and Min Zou. Micro/nano engineering on stainless steel substrates to produce superhydrophobic surfaces. *Thin Solid Films*, 520:1520–1524, 2011.
- [88] Xinjian Feng, Lin Feng, Meihua Jin, Jin Zhai, Lei Jiang, and Daoben Zhu. Reversible Super-hydrophobicity to Super-hydrophilicity Transition of Aligned ZnO Nanorod Films. *J. Am. Chem. Soc.*, 126(1):62–63, 2004.
- [89] C. Cachet and R. Wiart. Influence of a perfluorinated surfactant on the mechanism of zinc deposition in acidic electrolytes. *Electrochim. Acta.*, 44(26):4743–4751, 1999.
- [90] Stephen J. Banik and Rohan Akolkar. Suppressing Dendritic Growth during Alkaline Zinc Electrodeposition using Polyethylenimine Additive. *Electrochim. Acta.*, 179:475–481, 2015.
- [91] Kohei Miyazaki, Akiyoshi Nakata, You Shin Lee, Tomokazu Fukutsuka, and Takeshi Abe. Influence of surfactants as additives to electrolyte solutions on zinc electrodeposition and potential oscillation behavior. *J. Appl. Electrochem.*, 46(10):1067–1073, 2016.
- [92] *Joint Commission on Powder Diffraction Standards, International Centre for Diffraction Data*, <http://www.icdd.com>, 2003.

- [93] M. Ruths, S. Lundgren, K. Danerlo, and K. Persson. Friction of Fatty Acids in Nanometer-Sized Contacts of Different Adhesive Strength. *Langmuir*, 24:1509–1516, 2008.
- [94] M. Ratoi, V. Anghel, C. Bovington, and H.A. Spikes. Mechanisms of Oiliness Additives. *Tribol. Int.*, 33:241–247, 2000.
- [95] Rahul Jain and Ranga Pitchumani. Facile Fabrication of Durable Copper Based Superhydrophobic Surfaces via Electrodeposition. *Langmuir*, 34(10):3159–3169, 2017.
- [96] Giusti Paolo, Lazzeri Luigi, Barbani Niccoletta, Lelli Letizia, De Petris Silvano, and Cascone Maria G. Blends of natural and synthetic polymers: A new route to novel biomaterials. *Macromol. Sy.*, 78(1):285–297, 1994.
- [97] Sergey Dorozhkin. Nanosized and nanocrystalline calcium orthophosphates. *Acta. Biomater.*, 6(10):715–34, 2009.
- [98] G. Helen Annal Therese, P. Vishnu Kamath, and G. N. Subbanna. Novel electrosynthetic route to calcium phosphate coatings. *J. Mater. Chem.*, 8(2):405–408, 1998.
- [99] Stephanie D. Huelin, Holly R. Baker, Erika F. Merschrod, and Kristin M. Poduska. Phase-selective electroprecipitation of calcium phosphate thin films at physiological temperatures. *Cryst. Growth. Des.*, 6(11):10–12, 2006.